Dome permeability and fluid circulation at La Soufrière de Guadeloupe implied from soil CO2 degassing, thermal flux and self-potential

Amelie Klein, David Jessop, Franck Donnadieu, Joanny Pierre, Roberto Moretti

Dome permeability and fluid circulation at La Soufrière de Guadeloupe implied from soil CO_2 degassing, thermal flux and self-potential

Amelie Klein[1*], David E. Jessop[1,2], Franck Donnadieu[1], Joanny Pierre[3], Roberto Moretti[4]

[1*]Université Clermont Auvergne, CNRS, IRD, OPGC, Laboratoire Magmas et Volcans, Clermont-Ferrand, F-63000, France.
[2]Institut de Physique du Globe de Paris, Université Paris Cité, CNRS, Paris, France.
[3]Observatoire Volcanologique et Sismologique de la Guadeloupe, Institut de Physique du Globe de Paris, Le Houëlmont, Gourbeyre, 97113, France.
[4]Department of Engineering, University of Campania "Luigi Vanvitelli", Via Roma 29, Aversa, 81031, Italy.

*Corresponding author(s). E-mail(s): amelie.klein@uca.fr;
Contributing authors: david.jessop@uca.fr; franck.donnadieu@uca.fr; joanny@ipgp.fr; roberto.moretti@unicampania.it ;

Orcid IDs
Amelie Klein: 0009-0009-1386-4119
David E. Jessop: 0000-0003-2382-219X
Franck Donnadieu: 0000-0001-8293-1340
Roberto Moretti: 0000-0003-2031-5192

Abstract

Quantifying subsurface fluid flows and related heat and gas fluxes can provide essential clues for interpreting the evolution of volcanic unrest in volcanoes with active hydrothermal systems. To better constrain the distribution of current

hydrothermal activity, we mapped diffuse soil CO_2 degassing, ground temperature and self-potential covering the summit of La Soufrière de Guadeloupe during 2022-23. We identify areas of fluid recharge and the zones and extent of major ascending hydrothermal flows. This paper provides a first estimate for summit ground CO_2 flux of $4.20 \pm 0.86\,\mathrm{t\,d^{-1}}$, representing about half the CO_2 emissions from the summit fumaroles. We find an extensive area of ground heating of at least $22\,250 \pm 6900\,\mathrm{m^2}$ in size and calculate a total ground heat flux of $2.93 \pm 0.78\,\mathrm{MW}$, dominated by a convective flux of $2.25 \pm 0.46\,\mathrm{MW}$. The prominent summit fractures exert significant control over hydrothermal fluid circulation and delimit a main active zone in the NE sector. The observed shift in subsurface fluid circulation towards this sector may be attributed to a changing ground permeability and may also be related to observed fault widening and the gravitational sliding of the dome's SW flank. Our results indicate that the state of sealing of the dome may be inferred from the mapping of hydrothermal fluid fluxes, which may help evaluate potential hazards associated with fluid pressurisation.

Keywords: hydrothermal unrest, monitoring, diffuse degassing structures, heat and CO_2 flux, subsurface permeability, fluid circulation

Acknowledgements

This study was supported by the Service National d'Observation en Volcanologie (FD, DJ), the Tellus-Syster program (DJ) by the Institut National des Sciences de l'Univers of the French Centre National de la Recherche Scientifique (CNRS-INSU) and the InVolc Graduate Track program of Université Clermont Auvergne. RM, formerly at IPGP-OVSG, acknowledges financial support from the project AO IPGP 2018 "Depth to surface propagation of fluid-related anomalies at La Soufrière de Guadeloupe volcano (FWI): timing and implications for volcanic unrest", which allowed to set early joint surveys of soil heat and CO2 fluxes. The authors are deeply grateful to the OVSG (Observatoire Volcanologique et Sismologique de Guadeloupe) staff for logistic support and scientific discussion. We further thank Claude Hervier at the Observatoire de Physique du Globe de Clermont-Ferrand (OPGC) for maintaining and calibrating the high-impedance voltmeter used for SP measurements, Tristan Didier for producing the thermal probes and Tommaso Boni for great support in the field. This is contribution no. 617 of the ClerVolc program of the International Research Center for Disaster Sciences and Sustainable Development of the Université Clermont Auvergne.

Declarations

The authors have no conflicts of interest to declare that are relevant to the content of this article. AK, DJ, FD and JP conducted fieldwork. AK performed all data analyses and prepared the manuscript. RM and DJ conceptualised the preliminary studies of joint soil and CO2 heat fluxes. DJ and FD supervised AK and helped prepare the manuscript. RM provided critical feedback on the project and its results. All authors revised the manuscript and agreed to its submission.

1 Introduction

A common definition of a volcanic hydrothermal system is an underground aquifer in a volcanic environment where hot and acid magmatic fluids discharged at depth interact with groundwater. These interactions typically manifest at the surface as fumaroles, thermal springs, hot acid lakes or boiling pools (Hochstein and Browne, 2000; Fischer and Chiodini, 2015). Hydrothermal fluid motion within a volcanic edifice is maintained by a quasi-constant supply of heat and gas from the magma reservoir into water circulating at shallower depths in the brittle, fractured and permeable host rock (Hedenquist and Lowenstern, 1994).

Convection of hydrothermal fluids can create a multitude of non-magmatic unrest signals, e.g. soil and fumarolic degassing, ground heating and deformation, volcano-tectonic seismicity (Rouwet et al, 2014; Pritchard et al, 2019). Additionally, hydrothermal systems modulate geochemical and geophysical signals of magmatic origin, making the interpretation of anomalies in monitoring data and consequently, eruption forecasting difficult (Barberi et al, 1992; Rouwet et al, 2014).

Hydrothermal fluids are enriched in the most water-soluble and acidic components of magmatic gases, e.g. SO_2, H_2S, HCl and HF (Hochstein and Browne, 2000; Fischer and Chiodini, 2015) promoting intense leaching and alteration (argillisation) of the host-rock. Host rock porosity/permeability is modified by alteration, either increasing or decreasing according to the type of alteration. Porosity-increasing alteration is thought to reduce rock strength and thus edifice stability (López and Williams, 1993; Watters et al, 2000; Farquharson et al, 2019; Heap et al, 2021b), whereas porosity-decreasing alteration (sealing) increases rock strength whilst simultaneously decreasing outgassing, impeding fluid circulation and heat transfer to the surface and enhances pore fluid pressurisation (Heap et al, 2019).

Alteration promotes edifice instability and increases the likelihood of (partial) flank collapses (López and Williams, 1993; Reid et al, 2001; Reid, 2004), potentially causing sudden decompression of the hydrothermal system and laterally-directed blasts (cf. c. 3100 years B.P. event at La Soufrière de Guadeloupe, Boudon et al, 1984; Soufrière Hills, Montserrat, 1997 Sparks et al, 2002). Pore pressurisation can furthermore increase volcano spreading (Heap et al, 2021a) known to promote flank collapses (van Wyk de Vries and Francis, 1997; Karstens et al, 2019) and lead to highly explosive phreatic/phreato-magmatic activity and associated pyroclastic density currents (Heap et al, 2019, 2021a).

Circulating hot fluids with excess electrical charge within the volcanic edifice are evidenced by ground thermal anomalies, increased soil gas emanation, and changes in electric potential at the surface. A widely used method to quantify subsurface fluid flow in volcano-hydrothermal zones and to outline the extent and state of hydrothermal systems is self-potential (SP) mapping (e.g. Massenet and Pham, 1985; Zlotnicki et al, 1994; Finizola et al, 2002; Barde-Cabusson et al, 2012; Brothelande et al, 2014). SP is a passive technique that measures the naturally occurring difference in electrical potential between two electrodes placed at the ground surface. SP signals can have a variety of origins, including electrochemically-generated potentials (redox potentials in ore bodies and contaminant plumes, ion diffusion due to concentration gradients; Jouniaux et al, 2009), potentials produced by thermoelectric effects (Nourbehecht, 1963; Corwin and Hoover, 1979) and electrokinetic (streaming) potentials generated by the

flow of water through a porous material. Whilst different mechanisms can coexist, theoretical considerations by Corwin and Hoover (1979) imply that streaming potentials are larger by about an order of magnitude than thermoelectric and electrochemical potentials and there is general agreement that streaming is the main cause of SP anomalies on active volcanoes (Massenet and Pham, 1985; Zlotnicki et al, 1994; Finizola et al, 2002, 2004; Aizawa, 2008; Aizawa et al, 2009; Barde-Cabusson et al, 2012). For a detailed explanation of how streaming potentials are generated, the reader may refer to the papers of Revil et al (1999), Revil (2002), and Jouniaux and Ishido (2012). In general, for typical pH conditions at active volcanoes, the presence of an electrical double layer at the interface between the host rock and the pore water will lead to a net transport of positive ions, and thus the generation of a positive electric potential in the flow direction of the pore water (Revil, 2002). Therefore, on many active volcanoes, positive SP anomalies on the order of a few hundred mV are observed in the summit (crater) area of the edifices or above flank fissures and vents due to the upwelling of hydrothermal fluids, while on the flanks the percolation of meteoric water produces negative anomalies (Finizola et al, 2004; Jouniaux and Ishido, 2012).

The convection of fluids from depth transports heat to the surface, particularly in a hydrothermal setting. Rising hydrothermal fluids are either emitted by fumaroles where the permeability of the subsurface is high and/or fracture networks form natural conduits to the surface (Stevenson, 1993) or by diffuse soil degassing in low-permeability zones. Given that H_2O is by far the most abundant chemical species at 90–95 wt.%, and that it has some of the largest values of heat capacity and latent heat of any fluid, transport by water is the dominant mode of heat transfer at hydrothermal systems (Harris, 2013; Fischer and Chiodini, 2015). In low-permeability zones, the condensation of steam at the near subsurface liberates significant amounts of heat that is then transported to the surface, leading to ground heating (Aubert, 1999; Harris et al, 2009; Gaudin et al, 2015) and the emission of gas species, mainly CO_2, which do not condense at near-atmospheric conditions given their very low solubility. Thus, if measurements of either i) the surface temperature (e.g. with a thermal camera) or ii) the soil temperature profile are performed, the heat flux can be estimated using the thermal properties of the soil. Both techniques have been used in various hydrothermal volcanic settings (e.g. Aubert, 1999; Lewis et al, 2015; Gaudin et al, 2016; Jessop et al, 2021). In contrast, soil CO_2 together with the CO_2/H_2O ratio (often derived from analyses of fumarole gas samples) can be used to estimate total heat flux in diffuse degassing zones (Chiodini et al, 2001, 2005). Hence, in many volcanic environments, diffuse CO_2 degassing correlates with soil temperature anomalies and SP maxima (Lewicki et al, 2003; Finizola et al, 2010; Byrdina et al, 2014). Combining measurements of CO_2 degassing and soil temperature with SP can provide information on subsurface permeability (controlled by inherent host rock properties, the presence of fault/fracture networks and alteration processes, Grobbe and Barde-Cabusson, 2019) and help to outline the geometry of the hydrothermal system and constrain fluid circulation (e.g. Matsushima et al, 1990; Finizola et al, 2002; Lewicki et al, 2003; Finizola et al, 2004; Brothelande et al, 2014).

As recently demonstrated by the deadly events at Mount Ruapehu (New Zealand, 2007 Kilgour et al, 2010), Ontake volcano (Japan, 2014, Maeno et al, 2016) and Whakaari (White Island, New Zealand, 2019, Dempsey et al, 2020), even purely steam-driven/hydrothermal eruptions can be very hazardous given

their sudden onset. Therefore, monitoring the spatial distribution and temporal evolution of hydrothermal signals at volcanoes with long-lived hydrothermal activity is critical to detect and interpret precursory signals of explosive activity.

This study focuses on La Soufrière de Guadeloupe (Lesser Antilles), an active andesitic volcano with a well-developed hydrothermal system, that has been showing signs of growing unrest (HCl-rich summit degassing, formation of new summit fumaroles, deformation, fracture opening, seismicity and increased ground heat flux on the summit) (Komorowski et al, 2005; Allard et al, 2014; Villemant et al, 2014; Tamburello et al, 2019; Moretti et al, 2020a; Jessop et al, 2021) since 1992.

Here we present for the first time combined mapping of self-potential (SP), subsurface ground temperature and soil diffuse CO_2 flux on the summit of La Soufrière dome. Interpolated maps of these data show the main zones of rain infiltration into the hydrothermal system and zones of ascending flows. From our data we estimate the heat loss at the summit and, further, the condensation depth of the ascending hydrothermal vapour, which indicates the ground permeability distribution. Our results allow us to infer spatial changes in shallow hydrothermal fluid flow and ground permeability.

2 Geological setting and background

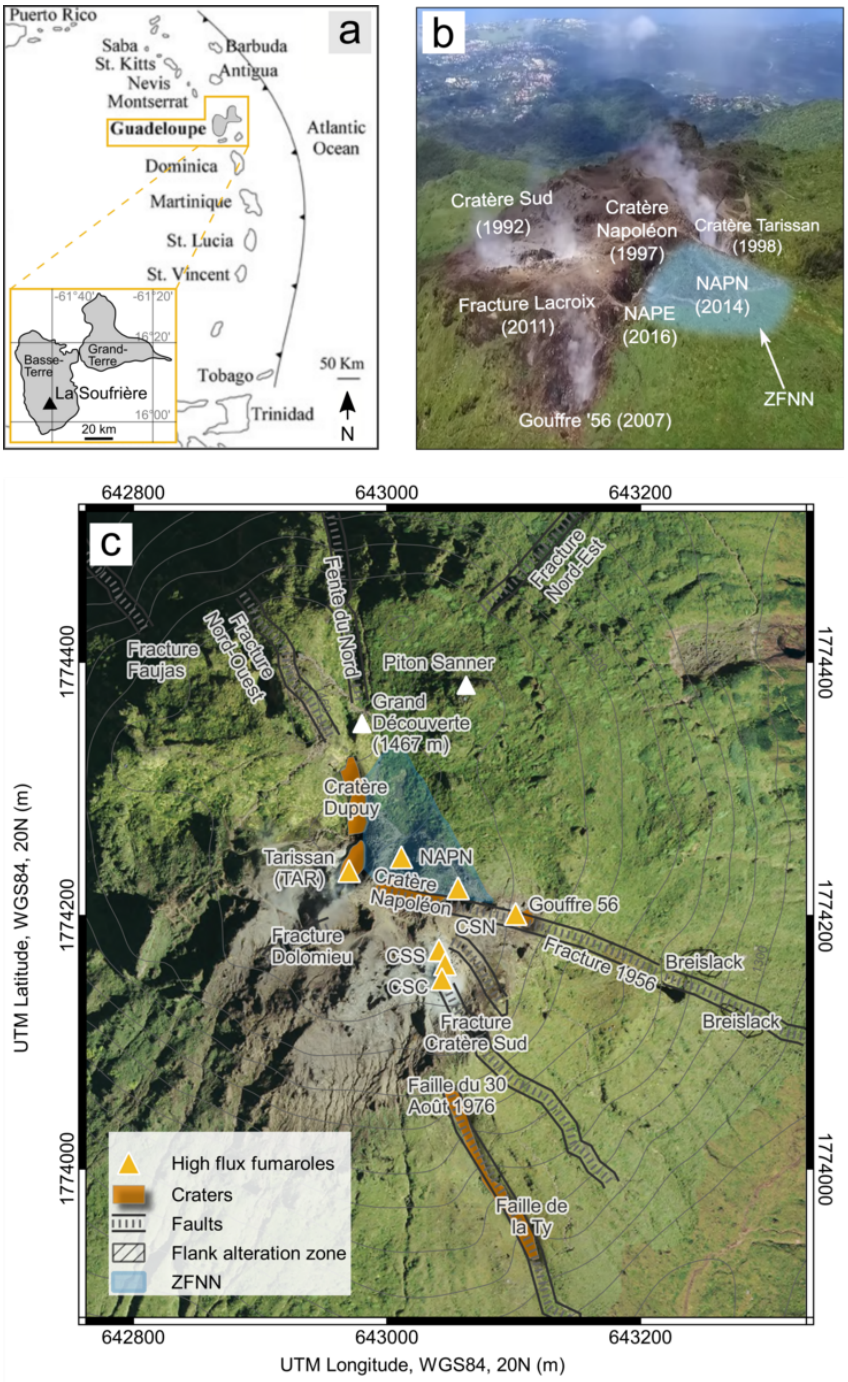

Fig. 1 (a) Schematic map showing the location of Guadeloupe in the Lesser Antilles arc and La Soufrière de Guadeloupe volcano in the southern part of Basse Terre island. Guadeloupe is situated in the central Lesser Antilles arc, where the Atlantic plate subducts under the Caribbean plate. Guadeloupe comprises two main islands: Grand-Terre, associated with the inactive outer arc and Basse-Terre, associated with the active inner arc (Adapted from Allard et al (2014); Pichavant et al (2018)). (b) Aerial photo (A. Anglade, OVSG-IPGP, 2016) of the summit area showing vegetation die-off due to acid degassing. Labelled are the main active fumaroles with the date of reactivation/appearance in brackets. NAPE and NAPN denote the Napoléon Est and Napoléon Nord fumaroles, respectively. The blue shading highlights the zone that has undergone recent changes in ground heating, degassing, and spreading (ZFNN: Zone Fumerollienne Napoléon Nord, since it spreads in the area around NAPN). (c) Map of the summit of La Soufrière de Guadeloupe showing the main geological features mentioned in the text. Main fumaroles indicated by the yellow triangles: Cratère Sud-Sud (CSS), Cratère Sud-Centre (CSC), Cratère Sud-Nord (CSN), Gouffre '56, Napoléon Est (NAPE), Napoléon Nord (NAPN), Tarissan (TAR). ZFNN (Zone Fumerollienne Napoléon Nord) denotes the recent spreading ground heating and diffuse degassing area. Isocontours (grey lines) are plotted every 20 m. The base map is the 2017 IGN aerial orthophoto (IGN, BD ORTHO 2017)

La Soufrière de Guadeloupe (16.0446° N, 61.6642° W, 1467 m a.s.l., hereafter referred to as La Soufrière) is an andesitic volcano situated in the central part of the Lesser Antilles island arc, where the North American plate subducts under the Caribbean plate (Feuillet et al, 2002). It is the youngest edifice of the Grande Découverte volcanic complex (445 kyr) on the southern Basse-Terre island of Guadeloupe and was emplaced during the last major magmatic eruption in 1530 AD (Boudon et al, 2008). Since this last magmatic event, extensive hydrothermal activity has persisted on and around the current lava dome and La Soufrière has experienced six phreatic eruptions, two of which were major events in 1797/98 and 1976/77 (Komorowski et al, 2005). Historic phreatic eruptions opened numerous (mostly radial) fractures and vents (Komorowski et al, 2005) on the dome whose evolution and degassing are routinely monitored and sampled by the Observatoire Volcanologique et Sismologique de Guadeloupe (OVSG-IPGP) along with seismic activity, surface displacements and weather conditions on the summit.

After the most recent and largest eruptive crisis in 1976/77, which led to the evacuation of more than 70 000 people and severe socio-economic problems for Basse-Terre (Komorowski et al, 2005; Hincks et al, 2014), the volcano became quiescent with only low-level fumarolic degassing along the Ty fault at the SW base of the dome (Zlotnicki et al, 1994) until 1992 when it entered a new unrest phase. Since 1992, degassing of summit fumaroles has been progressively increasing (year of fumarole reactivation indicated in Fig. 1b), concurrently with shallow seismicity, ground deformation, emission of chlorine-enriched acid gases, reactivation of thermal springs at the base of the dome, fumarole and ground temperature and the formation of boiling acid ponds at Cratère Sud (CS) (consisting of 3 vents aligned along a fracture: Cratère Sud Sud/Centre/Nord, CSS/CSC/CSN, 1997-2003, see Fig. 1) and Cratère Tarissan (TAR, since 2001, Fig. 1 and see also Zlotnicki et al (1992); Komorowski et al (2005); Villemant et al (2014); Rosas-Carbajal et al (2016); Moretti et al (2020a)).

Until 2014 soil degassing and ground thermal anomalies on the summit were limited to the areas directly surrounding the major fumaroles (i.e. CS, TAR, Cratère Napoléon, see Fig. 1 and Allard et al, 2014; Gaudin et al, 2016; Tamburello et al, 2019). However, the area affected by degassing and ground heating has been expanding in recent years and new high-flux fumaroles have appeared: Napoléon Nord, NAPN, in 2014 and Napoléon Est, NAPE, in 2016 (see Fig. 1 OVSG-IPGP 2014–2023[1] and Moretti et al, 2020a). Observed changes are particularly strong in an area around NAPN named the Zone Fumerolienne Napoléon Nord (ZFNN) delimited to the west by Cratère Dupuy and TAR (Fig. 1). In that zone, vegetation die-off has been extending concomitant with increased ground heat output (OVSG-IPGP 2014–2023 and Jessop et al, 2021).

The first mapping and estimation of La Soufrière heat and mass fluxes was carried out in 2010 (Gaudin et al, 2016). Jessop et al (2021) performed a recent analysis of the total heat flux discharged by the volcano (integrating data spanning 2000–2019) and compared estimated heat and mass fluxes for 2010 and 2019. The main change observed over this period is the emergence of the ground thermal anomaly at the summit, the ZFNN, which has led to an increase in ground heat flux by an order of magnitude (2010: 0.2 ± 0.1 MW, 2019: 5.7 ± 0.9 MW). Together with the appearance of new fumaroles (NAPN, NAPE) as well as extensive vegetation die-off on the summit, the total volcanic heat output was estimated to

[1] http://www.ipgp.fr/fr/ovsg/bulletins-mensuels-de-lovsg

have increased from 29.8 ± 8.3 MW in 2010 to 36.5 ± 7.9 MW in 2020 (Jessop et al, 2021).

A peak in unrest in 2018 (ML 4.1 earthquake) was interpreted as being the result of an increased supply of magma-derived fluids to the hydrothermal system, whose pressure build-up could be released since the dome was sufficiently permeable/fractured (Moretti et al, 2020a). Extensive hydrothermal activity at La Soufrière is sustained by heat and gas fluxes from a 6–7 km deep (i.e. below the summit) andesitic magma reservoir (Feuillard et al, 1983; Hirn and Michel, 1979; Allard et al, 2014; Pichavant et al, 2018; Metcalfe et al, 2022) to the deep aquifer (i.e. ≈ 1 km b.s.l. or 2.5 km below the summit) (Moretti et al, 2020a, and references therein). Deep, boiling hydrothermal fluids and magma-derived gases then rise through fractures, interact with groundwater at shallower depths (average rainfall summit: 5–6 m yr^{-1}, (OVSG-IPGP, 2012–2023) and feed summit fumaroles (Villemant et al, 2014; Moretti et al, 2020a; Moune et al, 2022). Shallow hydrothermal activity (i.e. ≤ 1.5 km below the summit) is considered responsible for the observed shallow deformation and seismicity (Moretti et al, 2020a) and increasing fluxes of rising acid fluids have caused extensive alteration (progressive sealing) and mechanical weakening of the dome (Komorowski et al, 2005; Salaün et al, 2011; Rosas-Carbajal et al, 2016; Heap et al, 2021b). These observations cause concern regarding the collapse of the SW flank, already showing surface displacements of up to 9 mm yr^{-1} towards the SW (Moretti et al, 2020a, OVSG-IPGP 1996–2023), which would not only directly affect the increasingly populated southern slopes, where more than 50 000 people reside, but could also decompress the hydrothermal system leading to explosive phreatic activity (Komorowski et al, 2005; Moretti et al, 2020a).

3 Methods

To better constrain the distribution of presently active hydrothermal zones on the dome, we have, for the first time, conducted self-potential, temperature and diffuse CO_2 flux surveys over a relatively short ≈ 1 year duration. SP and temperature measurements were carried out at the summit area of La Soufrière (Fig. 1) during a field campaign in May/June 2022 under overall constant, humid weather conditions but without any major rainfall. Due to instrument issues in 2022, soil CO_2 flux (ϕCO_2) data were acquired during another campaign in May 2023 under mostly dry weather conditions. All the data were located using a handheld GPS receiver (Garmin eTrex® 20 and Garmin GPSMAP® 60) as well as internal GPS in the CO_2 flux meter. To facilitate data analysis, all data sets were interpolated using the sequential Gaussian simulation (sGs) algorithm within the open-source Stanford Geostatistical Modeling Software (SGeMS) (Remy et al, 2009) and following the methods of Cardellini et al (2003). 250 simulations were performed for each data set using simulation grids with 5 m node spacing. The variograms of the normal score transformed data and fitted variogram models can be found in Fig. 10. The produced realisations were post-processed to obtain E-type (E: expected value) maps. The E-type map, i.e. the map of the mean at all grid nodes, is obtained through pointwise linear averaging of all the realisations. The maps of E-type (mean) are reported in Fig. 2, 4, 6, 9; they were used to calculate the reported heat and CO_2 fluxes and to define the extent of the heated and diffuse degassing area.

3.1 Temperature profiles, gradient and heated area calculations

Temperature data were acquired at a mean spacing of 11 m (maximum of 48 m), with a generally higher density of data points east of Cratère Dupuy and TAR. Ground temperatures were measured along vertical profiles at the surface, at 20 and 60 cm depth using three PT100 platinum resistance thermometers (measurement accuracy ±1 °C) embedded in a thermal paste in stainless-steel, ground-penetrating spikes. The thermal probes, built at the OVSG-IPGP, were connected to a portable data logger that took readings in real-time at 1 Hz. Before each temperature measurement, we hammered a steel bar (approx. 2 cm diameter) into the ground to the respective depths. We then inserted the thermal probes into the holes created and took readings when the temperature had stabilised. Error on the depth of probe insertion was less than 5 cm.

We obtained estimations of temperature variation with depth x using a linear model

$$T(x) = ax + b, \tag{1}$$

where $dT/dx = a$ is the prediction of the temperature gradient and $T(0) = b$ is the predicted surface temperature. For each measurement site, we estimated the coefficients a and b using a weighted linear least-squares method, with weights derived from the uncertainty of depth measurements (typically ±0.5 cm).

We calculated the heated area from the interpolated map shown in Fig. 4 using the threshold of the background temperature, $T_{\text{background}} = 22\,^{\circ}\text{C}$ (cf. Fig. 3). This procedure yielded a binary image where the non-zero pixels represented the heated area. The heated area is thus the number of non-zero pixels multiplied by the resolution of the sGs map, 25 m^2. To obtain an error bound on the calculated heated area, we considered that the natural isotherm is discretised by the perimeter of the heated area and will cut through the pixels of the boundary. Thus we calculated the discrete heated area perimeter using a Laplace edge-detection algorithm with a 3-pixel kernel. The number of perimeter pixels again multiplied by the image resolution plus the standard deviation of the ground temperature from the 250 realisations gives our error bound.

3.2 CO_2 measurements

We performed soil diffuse CO_2 degassing measurements following the accumulation chamber method as described in detail by Chiodini et al (1998). This is an established method for measuring soil CO_2 flux in volcanic areas, whose reliability has been tested both under laboratory conditions and in the field (e.g. Chiodini et al, 1996, 1998; Cardellini et al, 2017). Specifically, we used a West Systems® flux meter attached to a type B accumulation chamber consisting of a cylindrical chamber (20 cm inlet diameter, 19.8 cm internal chamber height), an IR spectrometer (LI-COR CO_2 detector LI-830 with accuracy within 3% of reading, and measurement range 0–20 000 ppm CO_2), and an AD converter. A Bluetooth-connected smartphone managed the flux meter. Chiodini et al (1998) report a reproducibility error of the accumulation chamber method of less than ±10 %, consistent with the manufacturer's (West Systems) stated measurement accuracy of ±10 % in high flux zones ($> 60\,\text{g}\,\text{m}^{-2}\,\text{d}^{-1}$) and ±25 % in low flux zones ($< 60\,\text{g}\,\text{m}^{-2}\,\text{d}^{-1}$). Our measurements were taken at a mean spacing of 15 m

(minimum of 3 m, maximum of 35 m). We were not able to perform measurements on a regular grid (cf. Cardellini et al, 2003) owing to the rugosity of the terrain, though we achieved a higher density of measurements within the ZFNN. The soil CO_2 flux is proportional to the concentration increase in the accumulation chamber over time (120–200 s per measurement). Flux values were derived from the slope of a linear fit of concentration as a function of time.

The diffuse CO_2 degassing area was calculated from the interpolated map shown in Fig. 6 using the median of our CO_2 data ($17.6\,g\,m^{-2}\,d^{-1}$) as the threshold for relevant CO_2 degassing. The CO_2 degassing area is thus the number of pixels with a CO_2 flux above $17.6\,g\,m^{-2}\,d^{-1}$ multiplied by the resolution of the sGs map, $25\,m^2$. The error bound of the degassing area was obtained following the same process as for the heated area. The estimated total uncertainty of the reported area accounts for the uncertainty of the perimeter of degassing pixels, uncertainty in the CO_2 measurement and the standard deviation of CO_2 flux from the 250 realisations.

3.3 Self-potential

SP values were taken at a mean spacing of 6 m (typical range 5–15 m, maximum spacing 29 m) over the summit area. The measuring equipment consisted of a digital voltmeter (10 GΩ input impedance, 1 mV sensitivity), two non-polarising $Cu/CuSO_4$ electrodes and a 500 m long insulated cable. Before starting the measurements, the electrodes were placed tip to tip to check for a voltage $\Delta U \leq 1$ mV and several SP measurements were performed in a small area around the reference location to ensure the correctness of the SP values. The electrodes were placed at a depth of 5–10 cm, which usually was enough to get good contact with the ground. All SP data were closure corrected following Barde-Cabusson et al (2021), distributing the drift (a few mV over the duration of 2–5 hours) linearly over the loops. Elevation changes are known to induce variations in SP readings due to vertical distance between the surface and the water table ('topographic effect'), typically leading to a negative linear relationship between SP and elevation in the hydrogeological zones (flanks) of active volcanoes (Lénat, 2007). Since we only measured on the summit and given the small elevation changes of < 40 m over our study area, this effect was minimal and we did not correct our data for topography-induced variations.

4 Results

4.1 Self-potential map of the summit

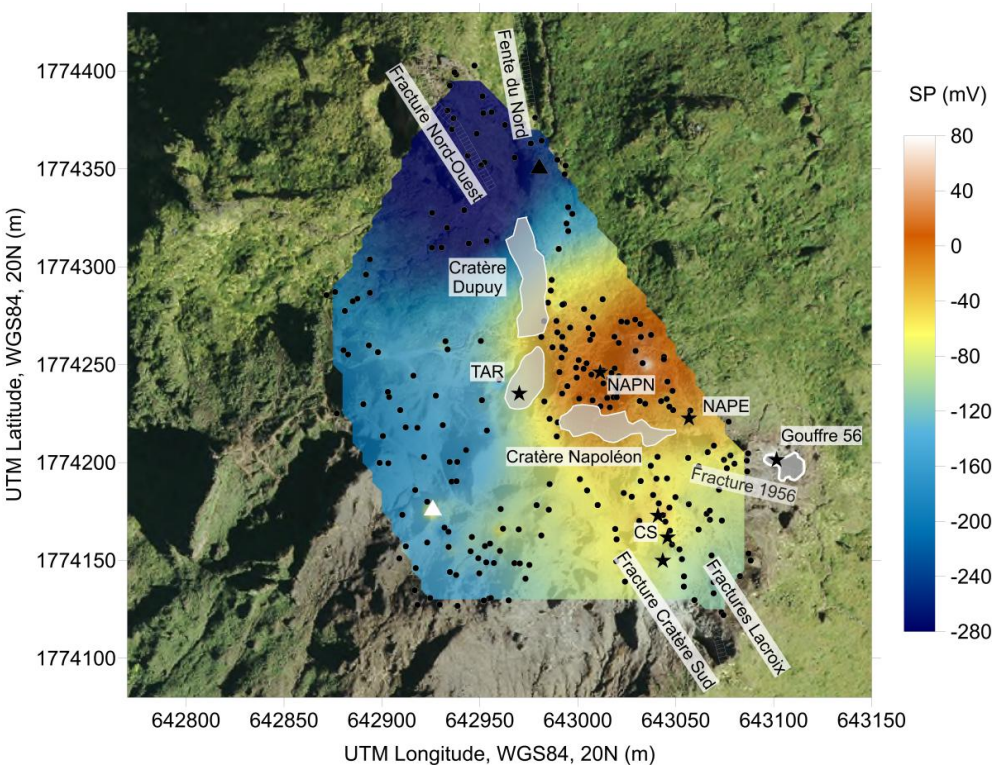

Fig. 2 Interpolated (sGs) map of self-potential (SP) superimposed on an orthophoto of the summit area of La Soufrière de Guadeloupe (background image is IGN, BD ORTHO 2017). The map shows the average SP of the 250 realisations in individual model cells (5 × 5 m). Black dots display the SP measurement points, the white triangle shows the location of the reference electrode. Stars indicate the main summit fumaroles: Cratère Sud (CS), Gouffre '56, Napoléon Nord (NAPN), Napoléon Est (NAPE) and Tarissan (TAR). The area east of Cratère Dupuy/TAR and north of Cratère Napoleon is denoted ZFNN (cf. Fig. 1b and c)

We performed SP measurements covering the entire summit area of La Soufrière to constrain zones of hydrothermal upwelling and rain infiltration, respectively. The resulting SP map (Fig. 2) shows an overall negative signal except for a localised area delimited by Fracture Napoléon to the south and Cratère Dupuy/-Tarissan to the west (ZFNN). This overall negative signal is expected on such a highly fractured and humid volcano, where meteoric infiltration is large (average annual rainfall 2016–2021: 4.5 m. OVSG-IPGP, 2016–2021; Vaerewyck, 2022).

The highest negative anomaly is located north of Cratère Dupuy where rocks at the surface are mostly unaltered and the vegetation is intact suggesting no

recent or past hydrothermal activity at the surface. Contrastingly, the southern areas of the summit contain surface rocks that are strongly argillised, implying lower ground permeability that could explain less negative SP than in the northern zone due to less effective rain infiltration. Moreover, we observe more negative values (range: -352 to -44 mV) west of Cratère Dupuy/TAR as opposed to the eastern part of the summit area, where values range between -270 and 84 mV. This is in agreement with the absence of fumaroles/ diffuse degassing west of Cratère Dupuy, whereas there are several sites of strong degassing in the eastern part of the summit (CS, NAPN, TAR, Gouffre '56), as well as diffuse degassing (ZFNN). Positive SP values are all located in the ZFNN. They suggest local ascent of hydrothermal fluids and relatively high ground permeability/fracturing. The positive anomaly extends to the edge of the vegetation in the east of the survey area. Given visible degassing and locally heated ground within the vegetation east of the surveyed area, it most probably also spreads into the vegetation, which is consistent with the observed progressing vegetation die off (OVSG-IPGP, 2014–2022).

4.2 Ground heating and temperature gradients at the summit

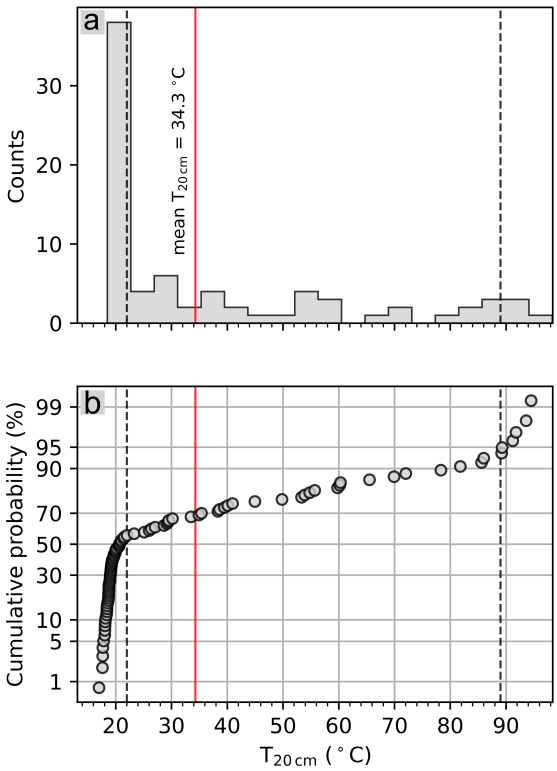

Fig. 3 (a) Histogram and (b) probability plot of the temperature data at 20 cm depth, as presented in Fig. 4a. From the distribution of these data, we identify three populations with cutoff temperatures of 89 and 22 °C, indicated by dashed black lines. The mean temperature at 20 cm depth is indicated by the red line

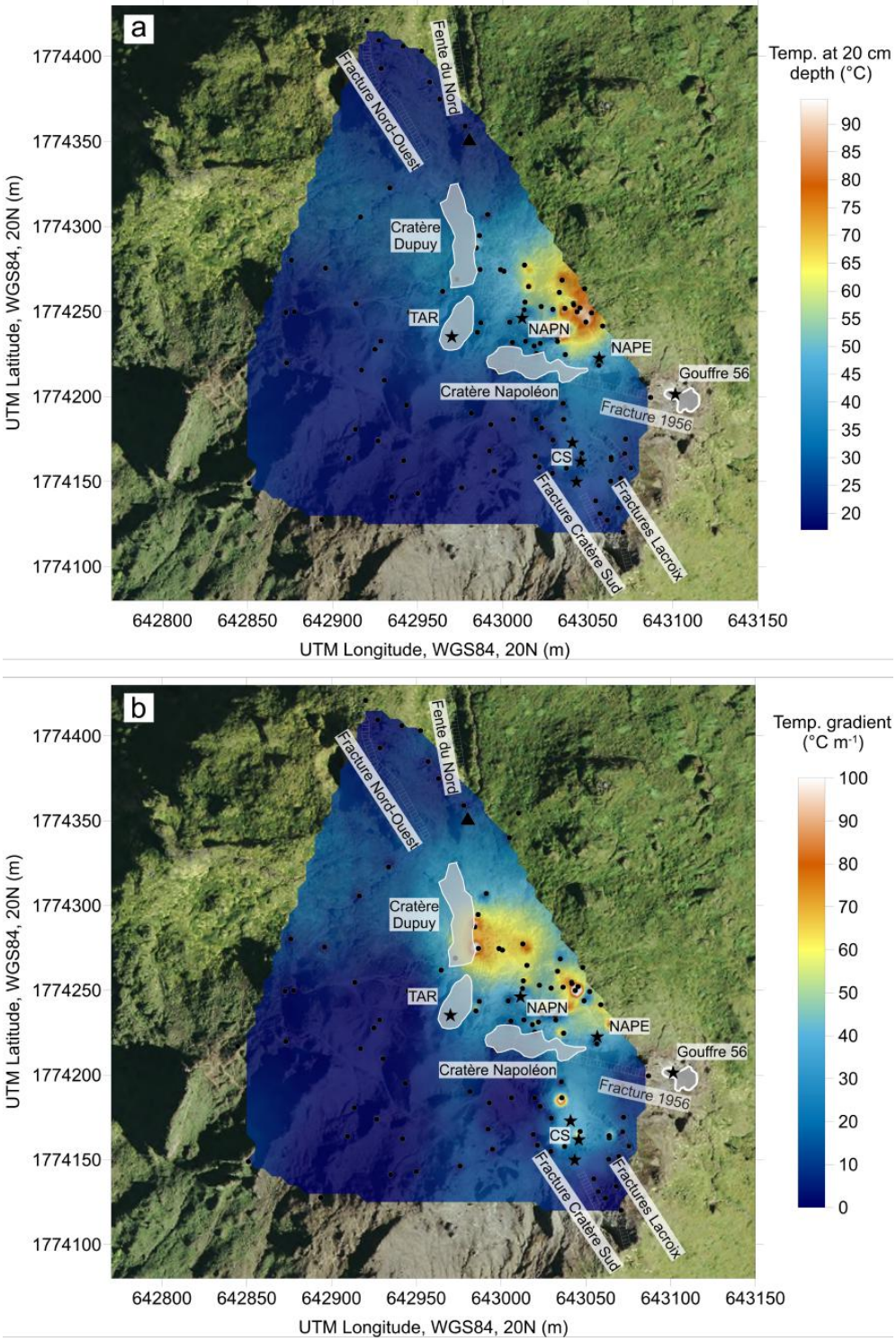

Fig. 4 Interpolated (sGs) maps of (a) ground temperature at 20 cm depth and (b) the ground temperature gradient calculated from (Eq. 1) and temperature measurements at 0, 20 and 60 cm depth. Shown are the mean values of the 250 realisations in individual model cells (5×5 m) superimposed on an orthophoto of the summit area of La Soufrière. Black dots display the locations of temperature measurements; stars indicate the main summit fumaroles: Cratère Sud (CS), Gouffre '56, Napoléon Nord (NAPN), Napoléon Est (NAPE) and Tarissan (TAR). The area east of Cratère Dupuy/TAR and north of Cratère Napoleon is denoted ZFNN (cf. Fig. 1b and c)

Measured ground temperatures (Fig. 4a) are highest in the ZFNN, reaching 94.5 °C at 20 cm depth. Away from craters and fractures, the ground temperature is close to ambient temperature (only minor effects of solar heating at 20 cm depth expected) varying between approx. 17 and 19 °C. The only exceptions are close to TAR/southern part of Cratère Dupuy (26.4–33.5 °C), around CS (ambient temperature to locally 35.4 °C) and in the ZFNN (20–94.5 °C). The highest temperatures are just below the boiling point of water at this altitude (95.2 °C), suggesting condensation of boiling hydrothermal fluids close to the surface.

We show the temperature gradient calculated from Eq. (1) in Fig. 4b. Spatially, we observe a similar distribution as per ground temperature. Away from fractures and the hydrothermally active areas, temperature gradients are essentially zero. There appears to be some structural control to the temperature gradients and we observe higher values ($> 50\,^{\circ}\mathrm{C\,m^{-1}}$) aligning with the major faults (CS/Fente du Nord and Fracture 1956). The highest gradients, i.e. beyond $90\,^{\circ}\mathrm{C\,m^{-1}}$ are found next to Cratère Dupuy, around CS and in the ZFNN with a maximum value of $161.50 \pm 55.12\,^{\circ}\mathrm{C\,m^{-1}}$ situated on the border between the ZFNN and Cratère Dupuy.

4.3 Soil CO_2 flux at the summit

In diffuse degassing areas, soil CO_2 flux often originates from biogenic or volcanic sources, resulting in a bimodal distribution of CO_2 flux values. In a logarithmic probability plot, this is represented as a curve with an inflection point from which background and volcanic populations can be partitioned following Sinclair's method (Sinclair, 1974; Chiodini et al, 1998). The absence of obvious inflexion points in the logarithmic probability plot (cf. Fig. 5b) implies a single lognormally-distributed population (Sinclair, 1974; Chiodini et al, 1998; Elío et al, 2016). This indicates that the measured CO_2 flux has a unique volcanic-hydrothermal source and that our data do not include any significant biogenic contribution.

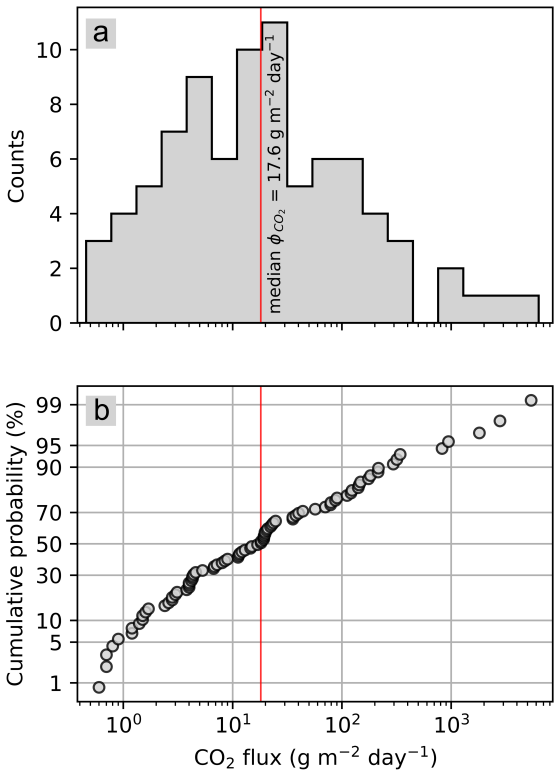

Fig. 5 (a) Histogram and (b) Log probability plot of the soil CO_2 flux data on the summit of La Soufrière. The absence of obvious inflexion points and linear alignment of data points implies a single lognormally-distributed (i.e. unimodal) population (Sinclair, 1974; Chiodini et al, 1998; Elío et al, 2016), indicating that measured CO2 flux has a unique volcanic-hydrothermal source and that our data do not include any significant background CO2 flux

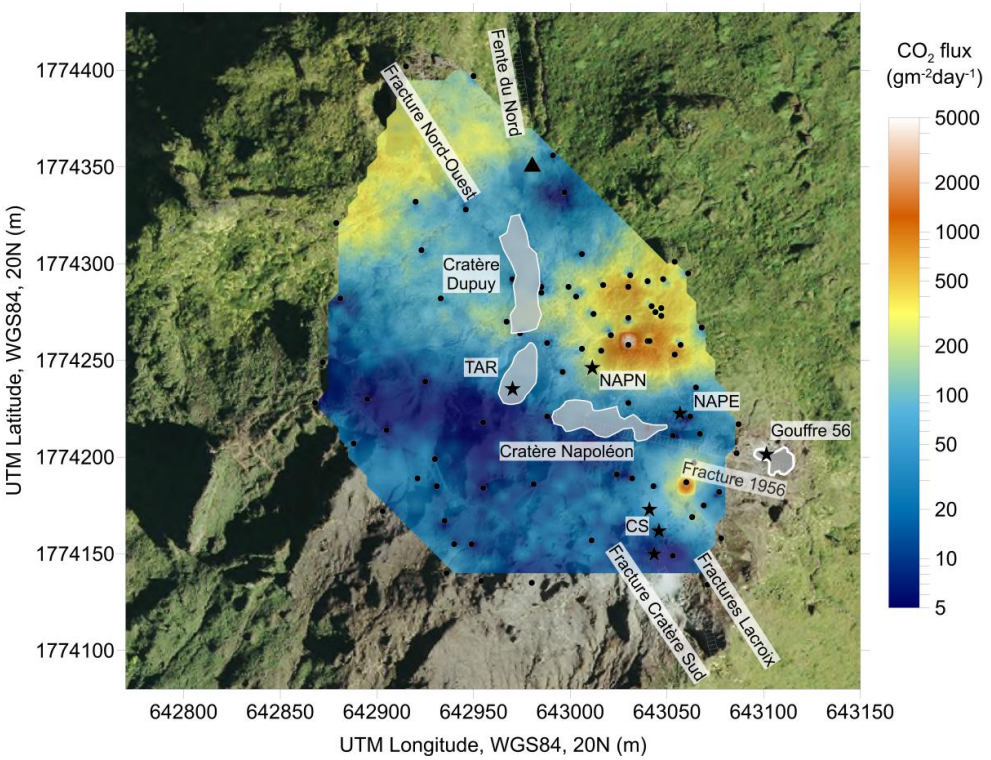

Fig. 6 Interpolated (sGs) map of soil CO_2 flux measurements in May 2023. The map shows the mean values of the 250 realisations in individual model cells (5×5 m) superimposed on an orthophoto of La Soufrière. Black dots indicate the locations of CO_2 flux measurements; stars indicate the main summit fumaroles: Cratère Sud (CS), Gouffre '56, Napoléon Nord (NAPN), Napoléon Est (NAPE) and Tarissan (TAR). The area east of Cratère Dupuy/TAR and north of Cratère Napoleon is denoted ZFNN (cf. Fig. 1b and c)

The distribution of soil CO_2 flux on the summit area of La Soufrière (Fig. 6) shows variations spanning four orders of magnitude ($0.6 \leq \phi CO_2 \leq 5390\,\mathrm{g\,m^{-2}\,d^{-1}}$). Like SP and temperature (gradient), CO_2 flux is highest in the ZFNN and in the vicinity of CS ($\phi CO_2 > 200\,\mathrm{g\,m^{-2}\,d^{-1}}$. CO_2 flux is also punctually increased ($\phi CO_2 > 100\,\mathrm{g\,m^{-2}\,d^{-1}}$ close to the large faults Fente du Nord and Fracture Nord-Ouest, although interpolation is based on very few points in the north of the survey area. CO_2 fluxes are low ($\phi CO_2 \leq 20\,\mathrm{g\,m^{-2}\,d^{-1}}$) everywhere else. As for SP and temperature, we find relatively sharp boundaries between areas of high and low ϕCO_2, implying that the ascent of hydrothermal fluids is controlled by the main fractures. More specifically, Cratère Dupuy/TAR (on the Fente du Nord - Faille de la Ty line) and Cratère Napoleon on the 1956 Fracture which delimit the ZFNN anomaly, and Fracture Cratère Sud and the Fractures Lacroix that control fluid ascent around CS.

Besides this structural control of fluid ascent along major summit faults and fractures, we note that also lithological interfaces and topography factors can exert control on the ascent pathways of fluids at volcanoes as described for La

Fossa cone, Vulcano (Schöpa et al, 2011). For example, preferential fluid migration might occur at the interface between rock units of different alteration states (and permeabilities) within La Soufrière dome (Rosas2016). However, the resolution of ERT data at La Soufrière (Rosas-Carbajal et al, 2016) is too low to infer any concrete ascent pathway based on alteration states within our survey area. Numerical modelling by Schöpa et al (2011) suggested that the gravitational stress field directs hydrothermal fluids to topographic highs, leading to the preferential occurrence of fumaroles at crater rims, a factor that might be at play in our survey area. The SP, temperature and CO_2 anomalies we observe may thus be associated with a combination of these factors.

5 Discussion

5.1 Spatial shift in hydrothermal fluxes evidenced by SP, ground temperature and soil CO_2

Comparison with previous SP studies at La Soufrière (Pham et al, 1990; Zlotnicki et al, 1994; Brothelande et al, 2014) suggests relative stability of the negative anomalies and thus the main infiltration zones over time. Nevertheless, there is an evolution of the positive anomalies on the summit. Pham et al (1990) found a negative anomaly covering the entire dome with the highest negative anomaly associated with the Faujas and NW fractures, in the northern part of the summit. This finding is consistent with the results of Zlotnicki et al (1994); Brothelande et al (2014) and this work. Concurrent with the reactivation of summit fumaroles beginning in 1992, Zlotnicki et al (1994) observed a positive anomaly from data acquired in 1993 in the southern sector of the summit, between Dolomieu Fracture and the 1956 Fracture, with a maximum just north of CS. This pattern was confirmed in 2011 by Brothelande et al (2014), who found a strong positive SP signal in the SE sector of the summit, a maximum near CS, and positive values stretching to the north until Cratère Dupuy (just south of Faujas and NW fracture; cf. Fig. 4B in Brothelande et al (2014)).

Qualitatively, we see a clear spatial shift in hydrothermal activity. While the area around CS and the entire SE summit sector still show higher values than the western part, we find a maximum anomaly in the ZFNN (just NE of Cratère Napoléon and stretching eastwards into the vegetation). Before 2014, ascending flows indicated by the SP maxima were only constrained to CS and its surroundings, as opposed to major activity in the ZFNN now.

We further note that even though positive and negative SP anomalies are generally interpreted as indicators for upward and downward fluid flow, respectively, this interpretation is not necessarily valid. The polarity of the SP anomalies essentially depends on the so-called zeta potential which describes the electric potential at the mineral-fluid interface in the porous rock and is a key parameter for electrokinetic coupling. The zeta potential is usually assumed to be negative in most Earth Science applications. In our case, the surface charge is compensated by a net positive, mobile charge in the pore fluid, which leads to the positive SP signal in the fluid flow direction. However, certain clay minerals and very acidic pore fluids (Revil, 2002; Hase et al, 2003; Aizawa, 2008; Jouniaux et al, 2009) can

result in positive or near zero zeta potentials. As a result, the sign of SP anomalies above ascending hydrothermal fluids may be reversed, or no significant SP anomaly may be observed.

As positive and negative potentials are always with respect to the reference point, a quantitative comparison between the various studies is not possible due to the reference electrode being in a different location in each one. Even though we placed our reference in an area with no hydrothermal activity, we do not consider it reasonable to recalculate our mapping to the reference at the base of the dome used by Brothelande et al (2014), given that more than a decade has elapsed between the two campaigns, during which the system has changed considerably. Given that our reference is located on the summit (c.f. Fig. 2) as opposed to the previous campaigns, the boundaries between positive and negative might not be comparable.

Since the pH of hydrothermal fluids sampled at the hot springs surrounding La Soufrière dome and on the summit (monthly sampling by OVSG-IPGP, 2020-2023) is mainly comprised between 2 and 6.5, we assume that the zeta potential is negative, and the sign of SP anomalies is not reversed. That the observed positive SP anomalies coincide with high CO2 and heat fluxes supports this assumption. Gases at some of the summit fumaroles and the acid point in TAR are however characterised by very acidic fluids (< 1) (OVSG-IPGP, 1992–2023; Inostroza et al, 2022). Therefore, in some zones on the summit and around the dome, ascending hydrothermal fluids may not be associated with a distinct positive SP signal as observed at Faille de la Ty at the southern dome base (Brothelande et al, 2014). SP should therefore be interpreted with caution and in combination with complementary methods.

From the interpolated temperature data (Fig. 4) and taking the cutoff temperature of 22 °C (cf. Fig. 3), we find a heated area of $22\,250 \pm 6900\,\mathrm{m}^2$ on the summit compared to $14\,070\,\mathrm{m}^2$ determined from 2019 aerial thermal imagery (Jessop et al, 2021). This suggests that the heated area outside the vegetated zone has expanded since 2019. In making this comparison, we are aware of the limitations of the two different techniques: aerial thermal images may capture additional hot spots in areas that cannot be reached on foot, and vegetation may obscure the thermal signal which is not a factor for the direct measurements as reported here. We also find that the heated area depends essentially on the choice of background temperature and interpolation method, so by defining 21 °C and 23 °C as ambient temperature instead of the chosen 22 °C, we get a heated area of $25\,750 \pm 7200\,\mathrm{m}^2$ and $19\,425 \pm 6200\,\mathrm{m}^2$, respectively. Kriging yielded an area estimate ($12\,400 \pm 3900\,\mathrm{m}^2$) much closer to the value reported by Jessop et al (2021). We further note that our temperature survey does not cover the ZFNN temperature anomaly entirely as we were unable to venture into densely-vegetated areas. Based on Fig. 4a) it is likely that the heated area in 2022 extended further to the E and NE into the vegetation and thus our estimate is a minimum value. This is supported by the fact that the SP anomaly reflecting the ascent of hydrothermal fluids in the ZFNN is likewise cut off at the eastern edge of the surveyed area (vegetation limit, Fig. 2) and by "hot mud" observed at several spots in the vegetation a few tens of meters east of the survey area.

Allard et al (2014) performed soil CO_2 degassing measurements using a portable Dräger IR spectrometer coupled to a West System accumulation chamber at the base of the dome and along a N–S profile on the summit in March

2006. They did not detect any ϕCO_2 anomalies on the summit that went beyond the biogenic background flux (60–160 $g\,m^{-2}\,d^{-1}$ in their study) except for a few spots around CS. However, we note that their study was conducted before the formation of the NAPN/NAPE fumaroles and the ZFNN.

In contrast to Allard et al (2014), we detected volcanic CO_2-flux not only in the vicinity of CS but also along TAR as well as in the ZFNN (Fig. 5b, Fig. 6), which is consistent with the formation of the fumarolic field on the dome summit since at least 2014. Using the median of our CO_2 data (17.6 $g\,m^{-2}\,d^{-1}$) as the threshold for relevant CO_2 degassing, we obtain a CO_2 degassing area of 26 220 $\pm$ 12 550 m^2. This value is consistent with the heated area estimate (22 250 $\pm$ 6900 m^2) and indicates the hydrothermally active area on the summit.

Overall, the high ground temperatures combined with maximum diffuse CO_2 flux and maximum SP values suggest strong hydrothermal fluid circulation below the ZFNN. The maximum SP, ground temperature, and CO_2 values are all located near 643 035 m E, 1 774 255 m N (UTM 20N - WGS84), about 25–40 m to the north-east of NAPN. We note that maximum values (T, soil CO_2 and SP) are delimited by prominent summit fractures: Fente du Nord, Dupuy and TAR to the west and Fracture 1956 /Cratère Napoléon to the south. Future efforts should be directed towards delimiting the eastern edge of subsurface fluid circulation. We interpret the concentration of activity in the NE sector of the summit as a result of increasing ground permeability, allowing hydrothermal fluids to rise through new fracture/pore networks. Increased ground fluxes/permeability in the NE sector may result from a combination of sealing processes affecting the location of increased heat and gas fluxes (proposed by e.g. Harris and Maciejewski (2000), Fossa fumarole field, Vulcano) and the observed opening of Cratère Napoléon (about 5 $mm\,yr^{-1}$ until 2023) (Moretti et al, 2020a, OVSG-IPGP 2018–2023) as well as radial surface displacements of 2.4–16.5 $mm\,yr^{-1}$ (OVSG-IPGP, 2023) on the summit. Extensometry data showed an accelerated opening of W–E fractures cutting the summit (Fracture Napoléon, Faille du 8 Juillet 1976, Breislack) between the end of 2015 and 2021, which is concurrent with the apparition of a new high-flux fumarole (NAPE, 2016) and several low-flux fumaroles scattered over the sector north of Fracture 1956 and east of Cratère Dupuy/TAR (OVSG-IPGP, 1992–2023). These observations could also be related to the sliding of the SW flank as indicated by GNSS velocities in Fig.7 in Moretti et al (2020a) associated with the alteration-induced detachment plane identified by Rosas-Carbajal et al (2016). Overall, these observations suggest a strong control of hydrothermal fluid circulation by the major summit faults /craters, which has also been shown to play an important role at La Fossa cone, Vulcano (Barde-Cabusson et al, 2009) and Aluto volcano, Main Ethiopian Rift (Hutchison et al, 2015). However, variations in lithology/alteration and the topography may influence surface permeability and the final distribution of hydrothermal anomalies at the surface (compare Schöpa et al (2011), La Fossa, Vulcano; Hutchison et al (2015), Aluto volcano, Main Ethiopian Rift).

5.2 Total soil CO_2 and heat fluxes

Integrating our ϕCO_2 data over the exhaling area, we find a total soil CO_2 flux of 4.20 $\pm$ 0.86 $t\,d^{-1}$. Moune et al (2022) found an average CO_2 flux for CS+Gouffre '56+TAR fumaroles in the 2018–2020 period of 0.094 $kg\,s^{-1}$ (8.13 $t\,d^{-1}$), meaning that diffuse degassing is equivalent to about half the CO_2 emissions from summit

fumaroles. Thus, diffuse degassing represents an important contribution to the CO_2 budget for La Soufrière de Guadeloupe.

We attempt to estimate the heat flux as

$$Q = \int_A (Q_{\text{cond}} + Q_{\text{conv}})\, dA, \tag{2}$$

where A is the survey area. The conductive heat flux, Q_{cond} is given by Fourier's law

$$Q_{\text{cond}} = k\,\frac{dT}{dx}, \tag{3}$$

where k is the thermal conductivity. Heap et al (2022) determined thermal conductivities for La Soufrière andesite according to their state of alteration and found $0.6\,\mathrm{W\,m^{-1}\,K^{-1}} \leq k \leq 1.6\,\mathrm{W\,m^{-1}\,K^{-1}}$ for highly-altered and low alteration rock. Thermal conductivity for partially-saturated unlithified samples from La Soufrière was found to be around $1\,\mathrm{W\,m^{-1}\,K^{-1}}$ (Heap et al, 2023), and such material was encountered at the majority of measurement sites. We use $k = 0.6\,\mathrm{W\,m^{-1}\,K^{-1}}$ and $k = 1.6\,\mathrm{W\,m^{-1}\,K^{-1}}$ in eq. (3) to calculate a typical value for Q_{cond} using the data shown in Fig. 4b) and find $Q_{\text{cond}} = 0.69 \pm 0.30\,\mathrm{MW}$, using the area covered by our ground temperature measurements.

However, as illustrated in Fig. 7, using a linear model to fit temperature gradients will systematically underestimate the surface gradient and thus the derived heat flux in areas with high hydrothermal fluxes. By way of example, using the data in Fig. 7 on the right, a linear fit to the ground temperature at all measured depths predicts $dT/dx \approx 45\,^{\circ}\mathrm{C\,m^{-1}}$. In contrast, a two-point gradient using the temperature at 0 and 10 cm depths, so only in the conductive zone, as indicated in Fig.6, gives $dT/dx \approx 450\,^{\circ}\mathrm{C\,m^{-1}}$. The actual conductive heat flux (cf. eq. (1)) would thus be significantly higher than our estimation with a linear fit over the entire depth, perhaps by as much as an order of magnitude.

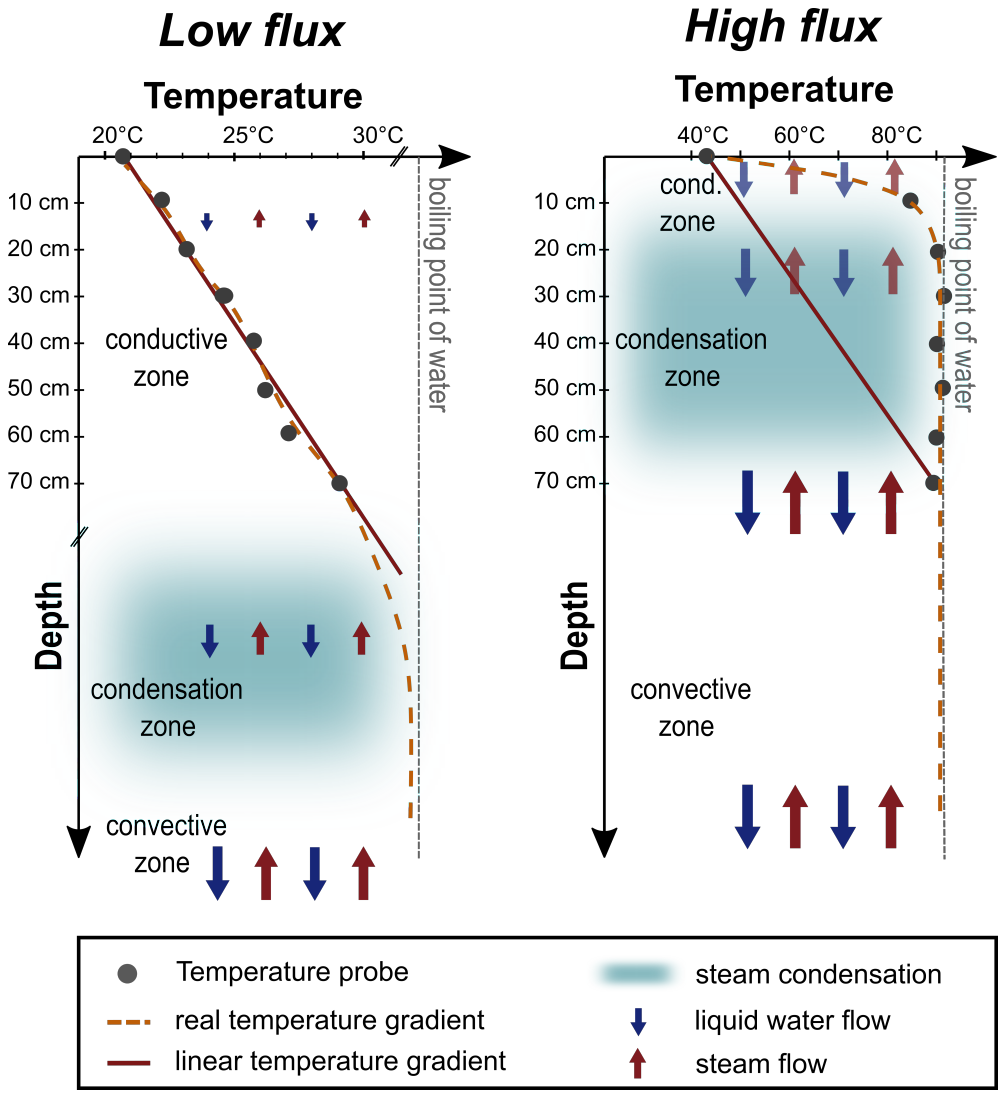

Fig. 7 Illustration of temperature profiles determined from the thermal probe measurements in low- and high-flux diffuse degassing areas. When the condensation zone is relatively deep, as in the left profile, heat is transported to the surface primarily by conduction (cf. eq. (3), and the estimated linear temperature gradient closely approximates the data. In high flux areas where the condensation zone is very shallow (right temperature profile), a linear gradient poorly approximates the data. Hence, our modelled linear temperature gradients lead to systematic underestimation of the derived surface heat flux using eq. (3) in high flux areas. The temperature profiles shown were measured (left) above Gouffre '56 (Easting: 643 084 m, Northing: 1 774 201 m; WGS84, UTM zone 20N) and (right) close to the NAPN fumarole (Easting: 643 013 m, Northing: 1 774 252 m) within the ZFNN. Figure adapted from Gaudin et al (2017)

The ground heat flux is due to fluids rising from depth. As discussed above, H_2O typically condenses beneath the surface and so cannot be readily measured whereas CO_2 is non-condensable at near-atmospheric P-T conditions. We estimate the steam flux, ϕ_{H_2O}, from the CO_2 flux by assuming that the hydrothermal H_2O/CO_2 mass ratio in diffuse degassing zones is the same as in fumarole vapours, since these result from the boiling of the deep hydrothermal aquifer (Moretti et al, 2020a). Given the small heat capacity of CO_2 compared to water and an average $H_2O/CO_2 = 17.8$ wt % (OVSG-IPGP, 2018–2023), heat transport by CO_2 is negligible compared to that transported by H_2O. Thus the convective heat flux is given by (Hochstein and Bromley, 2005; Fridriksson et al, 2006):

$$Q_{\text{conv}} = \int_A \frac{H_2O}{CO_2}\, \phi CO_2\, (h_{v,95} - h_{l,19})\, dA. \tag{4}$$

Here, $h_{v,95} = 2668\,\text{kJ}\,\text{kg}^{-1}$ is the specific enthalpy of steam at 95 °C (condensation temperature at summit level) and $h_{l,19} = 83\,\text{kJ}\,\text{kg}^{-1}$ the specific enthalpy of liquid water at ambient air temperature (19.1 °C) (Koretsky, 2012). Using Eq. (4) with the data presented in Fig. 6, we estimate $Q_{\text{conv}} = 2.25 \pm 0.46$ MW.

Thus by Eq. (2), we estimate that the total ground heat flux (i.e. $Q_{\text{cond}} + Q_{\text{conv}}$) is 2.93 ± 0.78 MW. We note that despite being only roughly half the value estimated by Jessop et al (2021) (5.7 ± 0.9 MW) from aerial thermal imagery as the sum of radiant and advective fluxes from the surface, our estimation is of the same order of magnitude and provides a lower bound for the "true" value. The study of Jessop et al (2021) covered a slightly larger area on the southern flank (about 100 m further south of CS) and in the densely vegetated zone to the east of the area investigated in this study (Fig. 4a). As far as the heated zones are concerned, the two studies cover approximately the same area. However, as described above, our temperature survey only partly covers the temperature anomaly in the ZFNN due to dense vegetation east of the surveyed zone. The aerial imagery of Jessop et al (2021) reached further to the east and thus may have captured additional heated spots despite the dense vegetation cover.

Our analyses can be put into a global context by considering how the heat and CO_2 budgets at La Soufrière compare to those for other volcanic complexes. To this end, we use the data set compiled by Harvey et al (2015) based on CO_2 degassing and plot them along with our data in Fig. 8. We find that La Soufrière's total heat output is larger only than that of the Comalito complex at Masaya but over a small area compared to the 22 other sites. However, large complexes such as calderas naturally have far larger total budgets hence the flux density is a fairer comparison between structures of different sizes (Harvey et al, 2015; Jessop et al, 2021). La Soufrière has mean heat and CO_2 flux densities of $132\,\text{MW}\,\text{km}^{-2}$ and $189\,\text{t}\,\text{km}^{-2}\,\text{d}^{-1}$, respectively. Based on heat flux density, these values are higher than for some large caldera-type complexes such as Solfatara, Campi Fleigri and Nisyros but below those of other dome-like structures such as Vulcano and White Island (Whakaari). The CO_2 flux density at La Soufrière is similar to that at Ischia and far higher again than at Nisyros.

As noted by Jessop et al (2021), the geological and volcano-tectonic setting will play a large role in determining these flux densities, along with the catchment area for reservoir recharge (Harvey et al, 2015). La Soufrière de Guadeloupe is indeed a volcanic dome associated with strong gas emissions that are related to the enhanced boiling activity of the hydrothermal reservoir and an

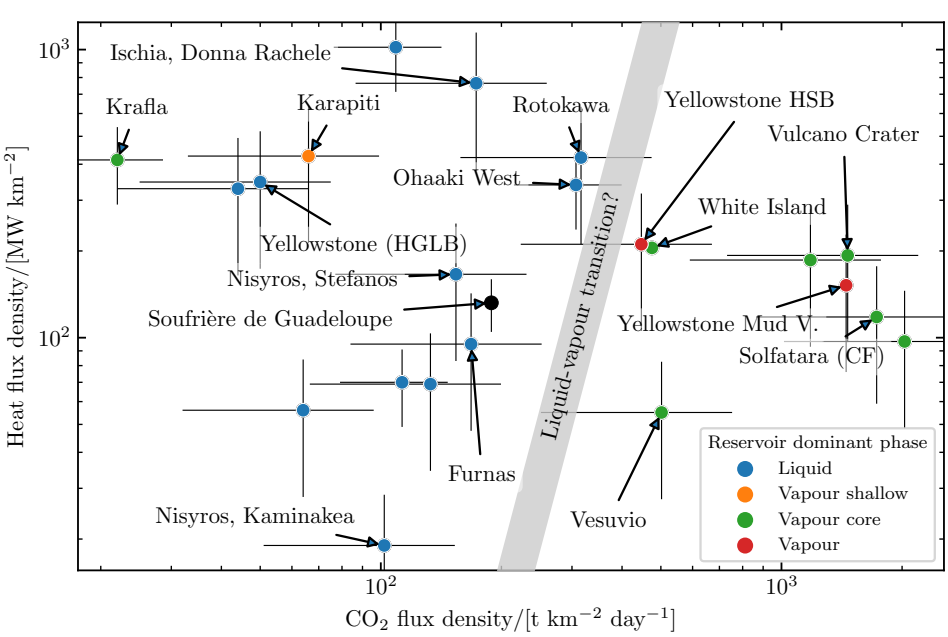

Fig. 8 Scatter plot of heat and CO_2 flux densities for a sample of hydrothermal volcanic systems. Here, the data (black dot: La Soufrière, this study; other data including error bars from Harvey et al, 2015) are classed in terms of the dominant phase in the reservoir (liquid/vapour). The grey bar indicates a suggested transition for the dominance of liquid to vapour. The slight top left to lower right trend for high heat flux/low CO_2 flux to low heat flux/high CO_2 flux is consistent with an increasing CO_2/H_2O ratio (see Fig. 1 in Harvey et al, 2015).

important proportion of hot magmatic gas vapour (Allard et al, 2014; Moretti et al, 2020a,b; Moune et al, 2022). Despite the low temperature of its fumarolic emissions which are close to the boiling temperature at the local height from La Soufrière's summit, Aiuppa et al (2017) include this volcano among high-temperature ($T \geq 450\,^{\circ}$C) arc volcanoes because of its high rate of emission and magmatic signature (C/S ≈ 2.3). Regarding the compilations provided by Harvey et al (2015) and Aiuppa et al (2017), we note that Fig. 8 includes White Island and Vulcano, also dome volcanoes, which both fall in the vapour-dominated region and display high-temperature ($T > 700\,^{\circ}$C) fumaroles. La Soufrière hydrothermal system is marked by P–T conditions which often approach the water critical point (Moretti et al, 2020a), and by the rapid transit of hot, deep magmatic gases (Allard et al, 2014; Moune et al, 2022; Metcalfe et al, 2023). Although sufficient to hydrothermally re-equilibrate acid species (e.g. CO_2, H_2S, SO_2, HF and HCl) these typically do not deplete the S-bearing species as is observed in mature hydrothermal systems dominated by the liquid. As a result, the high flux, low-temperature steam discharges do not indicate a large hydrothermal system close to the maturity condition typically marked by mofete-like emissions at about 100 °C, nor a vast and deep liquid reservoir in which acid gases of magmatic origin are efficiently scrubbed, obliterating the magmatic source signature. Instead,

as also shown by isotopic measurements (e.g. Villemant et al 2014), the high flux, low-temperature steam released at La Soufrière reflects the considerable contribution of meteoric water due to the heavy rainfall of a tropical environment (OVSG-IPGP, 1992–2023). We thus conjecture that rain saturation at the La Soufrière volcanic-hydrothermal system is responsible for its closeness to the inferred liquid-vapour transition. Furthermore, without such a contribution, La Soufrière would likely fall into the vapour-dominated region, at higher values of CO_2 flux density, due to the relatively lower absorption in circulating ground waters and water droplets in the soil.

5.3 Spatial variations in the dominant mode of heat transport and depth of condensation imply spatially heterogeneous permeability

From the temperature profiles calculated above, we can estimate the depth at which the vapour begins to condense, x_c, from the root of

$$T(x) - T_c = 0, \tag{5}$$

where $T(x)$ given by Eq. (1) and $T_c \approx 95\,^{\circ}\mathrm{C}$ which we solve using Newton's method. We also note that many sites have approximately zero temperature gradient, a, inferring that $T \ll T_c$. We interpret this as meaning that condensation will not occur in the near subsurface (i.e. in the first few metres). Where the gradients were approximately zero, we dropped these from our data set and interpolated the remaining values (59 out of 110 values). From the result, shown in Fig. 9, we note that x_c is on the order of a few tens of cm in the ZFNN and above the Fractures Lacroix, and increases to many metres elsewhere.

In areas where condensation occurs at depths greater than our measurements, one would expect heat transport by pure conduction, resulting in a linear temperature profile (constant gradient). Thus, one way to discriminate between the relative effects of conductive and convective heat transfer is to determine the linearity of the temperature profile. We do this by calculating Pearson's R^2 coefficient of determination from the linear regression of temperature with depth (cf. Ricci et al, 2015). The R^2 value measures how well a linear (i.e. conduction) model captures the data. Thus, $R^2 = 1$ where heat transfer is purely conductive whereas low values of R^2 indicate that convection is the dominant mode of heat transport. Our results are shown in Fig. 9 along with the interpolated map of condensation depths. From the combination of these data, we determine that the condensation isotherm in the ZFNN is very close to the surface. To the east of NAPN (specifically in the quadrant east of 643 010 m E and north of 1 774 225 m N in the local UTM), the profiles are typically linear: over 50% of this subpopulation of measurement sites have $R^2 > 0.925$. However, the other half of the population has $0.6 < R^2 < 0.925$ (see Fig. 9) indicating that convection is an important mode of heat transport in this region. This also becomes clear when comparing Fig. 4a) and Fig. 4b): while the temperature gradient in the above-mentioned quadrant is relatively small in many parts ($<45\,^{\circ}\mathrm{C\,m^{-1}}$, especially at the easternmost boundary of the quadrant), the measured ground temperatures at 20 cm depth range between 60 and 94.5 °C. Temperature gradients there are small because convection and the associated near-surface condensation (cf. Fig.

7) result in high ground temperatures up to the surface (reflected in the relatively low R^2 values mentioned). In other areas, either the profiles are close to linear or the condensation depth is very deep (cf. the western portion of our measurement sites) which indicates that conduction is dominant.

We are aware that basing the R^2 on only 3 data points (versus 4 data points in Ricci et al 2015) limits the robustness of our analyses. However, since we are not interested in the exact R^2 value, but only in the deviation from linearity, we still consider this method valid to get an idea of the spatial variations of the conductive versus convective heat transfer mode. This is supported by the fact that the distribution of calculated R^2 values is consistent with what we see from our SP, CO_2 and temperature data.

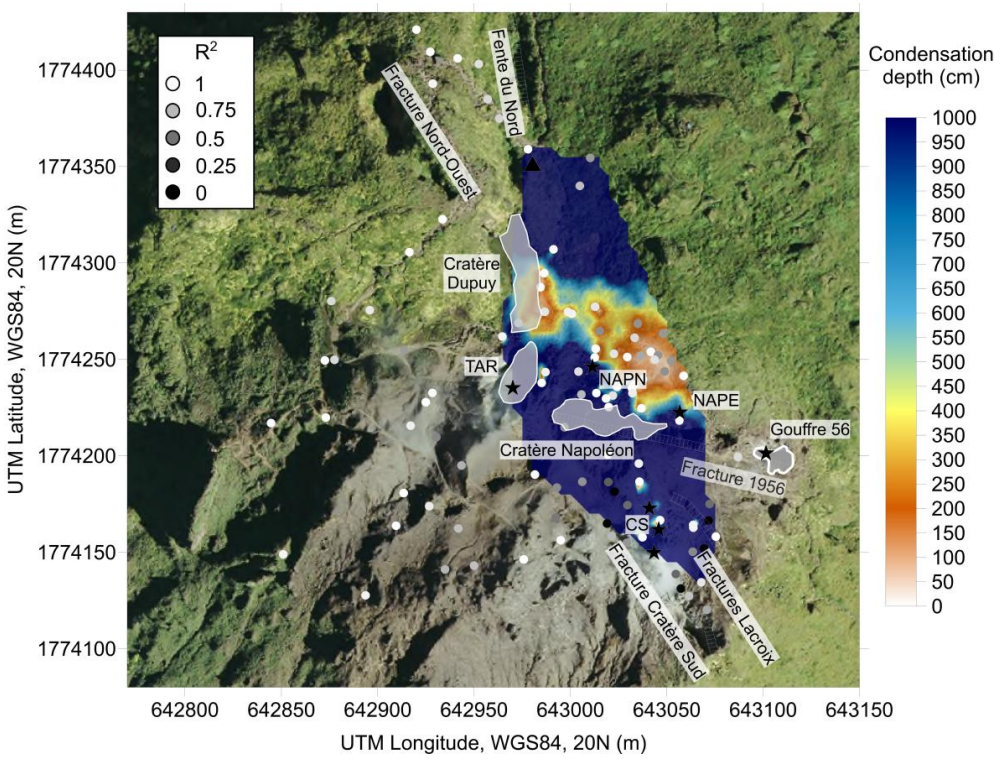

Fig. 9 Interpolated (sGs) map of condensation depths estimated from Eq. (5) overlain by the local value of Pearson's R^2 coefficient of determination. The R^2 value is used as an indicator of how well a linear temperature model describes the data, allowing us to discriminate between the relative effects of conductive and convective heat transfer(cf. Ricci et al, 2015). $R^2 = 1$ means that heat transfer is purely conductive, whereas low values of R^2 indicate an essential contribution of convection. The map shows the mean values of the 250 realisations in individual model cells (5×5 m) superimposed on an orthophoto of La Soufrière. Points at which temperature gradients were approximately zero were excluded from the estimation of condensation depth. No value indicates that the condensation depth is beyond 10 m. Black stars indicate the main summit fumaroles: Cratère Sud (CS), Gouffre '56, Napoléon Nord (NAPN), Napoléon Est (NAPE) and Tarissan (TAR). The area east of Cratère Dupuy/TAR and north of Cratère Napoleon is denoted ZFNN (cf. Fig. 1b and c)

The combination of these results supports the hypothesis (cf. 5.2) that high ground temperatures, diffuse CO_2 fluxes and SP values in the ZFNN might be due to increased ground permeability. Increased subsurface permeability promotes vapour condensation near the surface and, owing to the high heat capacity and latent heat of water vapour, increased heat transport and more extensive ground heating (compare Fig. 4). That few temperature anomalies are seen near the major fumaroles (CS, G56 and Tarrisan) is in keeping with the hypothesis of impermeable sealing by deposits of sulphur-bearing minerals (Moune et al, 2022).

Heap et al (2021b) sampled rocks from various locations on La Soufrière to study the degree of alteration and porosity of rocks forming the dome. They did not sample any rocks directly in the ZFNN; however, from our observations, the rock and soil in the ZFNN essentially correspond to what is also prevalent at the summit sampling locations of Heap et al (2021b). Rocks sampled close to summit fumaroles (Cratère Sud, Fractures Lacroix) showed secondary mineral assemblages typical for intense acid fluid-rock interaction promoted by the efficient circulation of hydrothermal fluids. They further found that sampled andesites from La Soufrière are more porous than andesites from other stratovolcanoes. This result is supported by muon (Lesparre et al, 2012) and electrical tomography (Rosas-Carbajal et al, 2016), which have indicated that the material forming the edifice has a low density and most probably comprises high-porosity rocks.

Seismic, geochemical and deformation data do not indicate any major changes in the magmatic-hydrothermal system (e.g. a rise in thermal input) but support the hypothesis that observed high ground temperatures, diffuse CO_2 fluxes and SP values in the ZFNN are due to alteration and/or increased ground permeability.

Seismicity is mainly superficial (typically <1 km below the summit) and can be interpreted as originating from the shallow hydrothermal system (Moretti et al, 2020a, OVSG-IPGP 2020–2023). GNSS and extensometry stations located on the summit and flanks of La Soufrière show a mainly radial deformation centred on Cratère Tarissan and an opening of Cratère Napoléon (about $5\,\mathrm{mm\,yr^{-1}}$ until 2023), related to the sliding of the SW flank of the dome (Moretti et al, 2020a, OVSG-IPGP 2018–2023). Deformation rates are essentially stationary and indicate no major change (inflation) in the deep system over the last ten years. The geochemical data also do not indicate a clear development in the magmatic system, although repeated injections of magmatic gases into the deep hydrothermal system (2–3 km below the summit) have been observed since 2018 (Moretti et al, 2020a; Moune et al, 2022, OVSG-IPGP 2018–2023). Instead, fumarole degassing rate and temperature are mainly regulated by the amount of water in the hydrothermal aquifer (Inostroza et al, 2022; Moune et al, 2022). A relatively low water level in the hydrothermal aquifer could contribute to the observed larger spatial extent of ground heating and CO_2 degassing at the summit due to reduced damping of reservoir/fluid temperature and CO_2 absorption by groundwater, but would not explain the increased fluid circulation in the ZFNN that our SP data suggests. However, lower precipitation in recent years (average annual rainfall 2016–2021: 4.5 m, Vaerewyck (2022) vs. 1983–2010: 10 ± 2 m, Villemant et al (2014)) may also affect soil thermal properties and permeability (Heap et al, 2020, 2023). While both the decreased water saturation of the system and increased permeability could play a role in the observed changes, it remains to be clarified which of the two factors is primary.

Future studies combining SP mapping with electrical resistivity tomography and possibly with induced polarisation tomography, as recently described in two reviews by Revil and Gresse (2021) and Revil et al (2023), could help to elucidate the structure of soil permeability further. The joint inversion of these data could provide valuable information about the depth and pattern of subsurface fluid flow as well as the current alteration state of the dome.

6 Conclusions

This paper presents the first combined mapping of SP, subsurface ground temperature and soil CO_2 flux on the summit of La Soufrière de Guadeloupe. These complementary methods allowed us to identify areas of fluid recharge into the hydrothermal system as well as the zones and extent of major ascending hydrothermal flows. A comparison of our data to previous work indicated spatial changes in shallow underground hydrothermal fluid circulation, which we explain with changing ground permeability distribution.

Based on our CO_2 flux measurements, we provide a first estimate of soil CO_2 degassing over the summit area, which amounts to $4.20 \pm 0.86\,\mathrm{t\,d^{-1}}$, about half the CO_2 emissions from summit fumaroles. These data further suggest a convective ground heat flux of $2.25 \pm 0.46\,\mathrm{MW}$ on the summit. Temperature gradients with depth derived from our soil temperature measurements allow us to get a lower bound estimate to conductive ground heat flux of $0.69 \pm 0.30\,\mathrm{MW}$ comprising minimum and maximum rock thermal conductivity values. We thus obtain a total summit ground heat flux (fumaroles not taken into account) of $2.93 \pm 0.78\,\mathrm{MW}$. We further determined the linearity of the temperature gradients with depth through Pearson's R^2 coefficient of determination, which along with the estimated condensation depths indicates that convection is an important mode of heat transport in the ZFNN (specifically in the quadrant east of 643 010 m E and north of 1 774 225 m N in the local UTM).

We find a heated (i.e. above ambient ground temperature) area of $22\,250 \pm 6900\,\mathrm{m^2}$ on the summit, suggesting that ground heating has expanded since 2019 (Jessop et al, 2021). Both our 2022 temperature and SP surveys seem to cut off the ZFNN anomaly at the eastern edge of the survey area where deep vegetation starts. It is thus likely that the heated area in 2022 extended further to the E and NE and we conclude that the value has to be considered a lower bound estimate and that future efforts should be directed towards delimiting the eastern edge of subsurface fluid circulation. In line with the heated area estimate, we find a ground CO_2 degassing area of $26\,220 \pm 12\,550\,\mathrm{m^2}$.

Maximum values of all measured parameters (CO_2 flux, ground temperature and SP) are located in the ZFNN indicating strong hydrothermal fluid circulation in that zone that we interpret as being a result of high sub-surface permeability. Comparison with previous studies shows that while the main rain infiltration zones seem to not have changed over time, we see a spatial development of the ascending flows. Repeated mapping will allow us to track the dynamic evolution of hydrothermal unrest and provide crucial information on the sealing extent of the dome.

The locations of flux maxima are delimited by prominent summit fractures: Fente du Nord, Dupuy and TAR to the west and Fracture 1956/Cratère Napoléon to the south. This implies a strong structural control of the observed dynamics

underlined by the gradual opening of the W–E fractures between 2015 and 2021. We thus speculate that the increase in hydrothermal activity in the ZFNN could be related to the observed radial surface displacements on the summit (OVSG-IPGP, 2023) and the sliding of the SW flank (Rosas-Carbajal et al, 2016; Moretti et al, 2020a).

7 Appendix

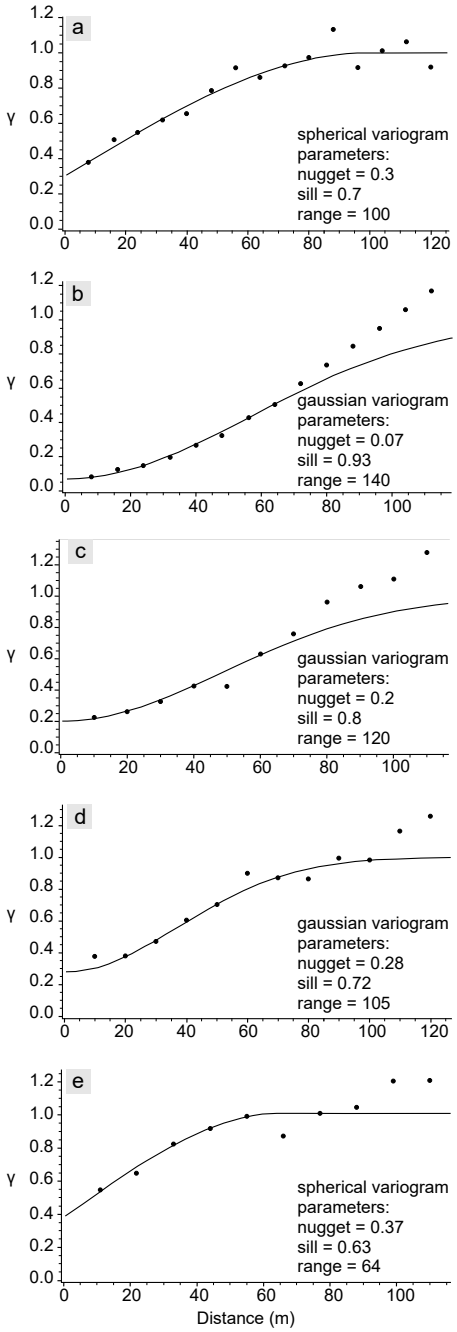

Fig. 10 Omnidirectional experimental variograms (γ) of normal score data: (a) soil CO_2 flux, (b) SP, (c) ground temperature at 20 cm depth, (d) ground temperature gradient, and (e) condensation depth. Lines represent the isotropic variogram models used in sGs interpolations. The outcome of the simulations is presented in Fig. 2, 4, 6, 9

References

Aiuppa A, Fischer TP, Plank T, et al (2017) Along-arc, inter-arc and arc-to-arc variations in volcanic gas CO_2/S_T ratios reveal dual source of carbon in arc volcanism. Earth-Science Reviews 168:24–47. https://doi.org/https://doi.org/10.1016/j.earscirev.2017.03.005, URL https://www.sciencedirect.com/science/article/pii/S0012825217300028

Aizawa K (2008) Classification of self-potential anomalies on volcanoes and possible interpretations for their subsurface structure. Journal of Volcanology and Geothermal Research 175:253–268. https://doi.org/10.1016/j.jvolgeores.2008.03.011

Aizawa K, Ogawa Y, Ishido T (2009) Groundwater flow and hydrothermal systems within volcanic edifices: Delineation by electric self-potential and magnetotellurics. Journal of Geophysical Research: Solid Earth 114(1). https://doi.org/10.1029/2008JB005910, URL https://agupubs.onlinelibrary.wiley.com/doi/abs/10.1029/2008JB005910

Allard P, Aiuppa A, Beauducel F, et al (2014) Steam and gas emission rate from La Soufriere volcano, Guadeloupe (Lesser Antilles): Implications for the magmatic supply during degassing unrest. Chemical Geology 384:76–93. https://doi.org/10.1016/j.chemgeo.2014.06.019

Aubert M (1999) Practical evaluation of steady heat discharge from dormant active volcanoes: case study of Vulcarolo fissure (Mount Etna, Italy). J Volcanol Geoth Res 92(3–4):413–429. https://doi.org/10.1016/S0377-0273(99)00088-8

Barberi F, Bertagnini A, Landi P, et al (1992) A review on phreatic eruptions and their precursors. Journal of Volcanology and Geothermal Research 52(4):231–246. https://doi.org/https://doi.org/10.1016/0377-0273(92)90046-G, URL https://www.sciencedirect.com/science/article/pii/037702739290046G

Barde-Cabusson S, Finizola A, Revil A, et al (2009) New geological insights and structural control on fluid circulation in La Fossa cone (Vulcano, Aeolian Islands, Italy). Journal of Volcanology and Geothermal Research 185(3):231–245. https://doi.org/https://doi.org/10.1016/j.jvolgeores.2009.06.002, URL https://www.sciencedirect.com/science/article/pii/S037702730900242X

Barde-Cabusson S, Finizola A, Peltier A, et al (2012) Structural control of collapse events inferred by self-potential mapping on the Piton de la Fournaise volcano (La Réunion Island). Journal of Volcanology and Geothermal Research 209-210:9–18. https://doi.org/https://doi.org/10.1016/j.jvolgeores.2011.09.014, URL https://www.sciencedirect.com/science/article/pii/S0377027311002575

Barde-Cabusson S, Finizola A, Grobbe N, et al (2021) A practical approach for self-potential data acquisition, processing, and visualization. Interpretation 9:T123–T143. https://doi.org/10.1190/int-2020-0012.1, URL https://hal.univ-reunion.fr/

hal-03003692

Boudon G, Semet MP, Vincent PM (1984) Flank failure–directed blast eruption at Soufrière, Guadeloupe, French West Indies: a 3,000-yr-old Mt. St. Helens ? Geology 12(6):350–353. https://doi.org/10.1130/0091-7613(1984)12⟨350:FFBEAS⟩2.0.CO;2, URL https://doi.org/10.1130/0091-7613(1984)12⟨350:FFBEAS⟩2.0.CO;2

Boudon G, Komorowski JC, Villemant B, et al (2008) A new scenario for the last magmatic eruption of La Soufrière of Guadeloupe (Lesser Antilles) in 1530 AD: evidence from stratigraphy, radiocarbon dating and magmatic evolution of erupted products. J Volcanol Geoth Res 178(3):474–490. https://doi.org/10.1016/j.jvolgeores.2008.03.006

Brothelande E, Finizola A, Peltier A, et al (2014) Fluid circulation pattern inside La Soufrière volcano (Guadeloupe) inferred from combined electrical resistivity tomography, self-potential, soil temperature and diffuse degassing measurements. J Volcanol Geoth Res 288:105–122. https://doi.org/10.1016/j.jvolgeores.2014.10.007, URL https://hal.univ-reunion.fr/hal-01391280

Byrdina S, Vandemeulebrouck J, Cardellini C, et al (2014) Relations between electrical resistivity, carbon dioxide flux, and self-potential in the shallow hydrothermal system of Solfatara (Phlegrean Fields, Italy). Journal of Volcanology and Geothermal Research 283:172–182. https://doi.org/https://doi.org/10.1016/j.jvolgeores.2014.07.010, URL https://www.sciencedirect.com/science/article/pii/S0377027314002212

Cardellini C, Chiodini G, Frondini F (2003) Application of stochastic simulation to CO2 flux from soil: Mapping and quantification of gas release. Journal of Geophysical Research: Solid Earth 108(B9). https://doi.org/https://doi.org/10.1029/2002JB002165, URL https://agupubs.onlinelibrary.wiley.com/doi/abs/10.1029/2002JB002165

Cardellini C, Chiodini G, Frondini F, et al (2017) Monitoring diffuse volcanic degassing during volcanic unrests: The case of Campi Flegrei (Italy). Scientific Reports 7. https://doi.org/10.1038/s41598-017-06941-2

Chiodini G, Frondini F, Raco B (1996) Diffuse emission of CO2 from the Fossa crater, Vulcano Island (Italy). Bulletin of Volcanology 58:41–50. https://doi.org/10.1007/s004450050124, URL https://doi.org/10.1007/s004450050124

Chiodini G, Cioni R, Guidi M, et al (1998) Soil CO2 flux measurements in volcanic and geothermal areas. Applied Geochemistry 13(5):543–552. https://doi.org/https://doi.org/10.1016/S0883-2927(97)00076-0, URL https://www.sciencedirect.com/science/article/pii/S0883292797000760

Chiodini G, Frondini F, Cardellini C, et al (2001) CO2 degassing and energy release at Solfatara volcano, Campi Flegrei, Italy. Journal of Geophysical Research: Solid

Earth 106(B8):16213–16221. https://doi.org/10.1029/2001JB000246, URL https://agupubs.onlinelibrary.wiley.com/doi/abs/10.1029/2001JB000246

Chiodini G, Granieri D, Avino R, et al (2005) Carbon dioxide diffuse degassing and estimation of heat release from volcanic and hydrothermal systems. J Geophys Res 110(B8):1–17. https://doi.org/10.1029/2004JB003542

Corwin RF, Hoover DB (1979) The self-potential method in geothermal exploration. GEOPHYSICS 44(2):226–245. https://doi.org/10.1190/1.1440964, URL https://doi.org/10.1190/1.1440964

Dempsey DE, Cronin SJ, Mei S, et al (2020) Automatic precursor recognition and real-time forecasting of sudden explosive volcanic eruptions at Whakaari, New Zealand. Nature Communications 11. https://doi.org/10.1038/s41467-020-17375-2

Elío J, Ortega M, Nisi B, et al (2016) A multi-statistical approach for estimating the total output of CO2 from diffuse soil degassing by the accumulation chamber method. Int J Greenh Gas Control 47:351–363. https://doi.org/10.1016/j.ijggc.2016.02.012

Farquharson J, Wild B, Kushnir A, et al (2019) Acid-induced dissolution of andesite: Evolution of permeability and strength. Journal of Geophysical Research : Solid Earth 124:257–273. https://doi.org/10.1029/2018JB016130, URL https://hal.science/hal-02376607

Feuillard M, Allegre C, Brandeis G, et al (1983) The 1975–1977 crisis of La Soufriere de Guadeloupe (F.W.I): A still-born magmatic eruption. Journal of Volcanology and Geothermal Research 16(3):317–334. https://doi.org/https://doi.org/10.1016/0377-0273(83)90036-7, URL https://www.sciencedirect.com/science/article/pii/0377027383900367

Feuillet N, Manighetti I, Tapponnier P, et al (2002) Arc parallel extension and localization of volcanic complexes in Guadeloupe, Lesser Antilles. Journal of Geophysical Research: Solid Earth 107(B12):ETG 3–1–ETG 3–29. https://doi.org/https://doi.org/10.1029/2001JB000308, URL https://agupubs.onlinelibrary.wiley.com/doi/abs/10.1029/2001JB000308

Finizola A, Sortino F, Lénat JF, et al (2002) Fluid circulation at Stromboli volcano (Aeolian Islands, Italy) from self-potential and CO_2 surveys. J Volcanol Geoth Res 116(1):1–18. https://doi.org/10.1016/S0377-0273(01)00327-4, URL https://hal.archives-ouvertes.fr/hal-01452542

Finizola A, Lénat JF, Macedo O, et al (2004) Fluid circulation and structural discontinuities inside Misti volcano (Peru) inferred from self-potential measurements. J Volcanol Geoth Res 135. https://doi.org/10.1016/j.jvolgeores.2004.03.009, URL https://hal.archives-ouvertes.fr/hal-01452539

Finizola A, Ricci T, Deiana R, et al (2010) Adventive hydrothermal circulation on Stromboli volcano (Aeolian Islands, Italy) revealed by geophysical and geochemical approaches: Implications for general fluid flow models on volcanoes. Journal of Volcanology and Geothermal Research 196(1-2):111–119. https://doi.org/10.1016/J.JVOLGEORES.2010.07.022, URL https://insu.hal.science/insu-00564998

Fischer TP, Chiodini G (2015) Volcanic, Magmatic and Hydrothermal Gases. In: Sigurdsson H (ed) The Encyclopedia of Volcanoes (Second Edition), second edition edn. Academic Press, Amsterdam, p 779–797, https://doi.org/https://doi.org/10.1016/B978-0-12-385938-9.00045-6, URL https://www.sciencedirect.com/science/article/pii/B9780123859389000456

Fridriksson T, Kristjánsson BR, Ármannsson H, et al (2006) CO2 emissions and heat flow through soil, fumaroles, and steam heated mud pools at the Reykjanes geothermal area, SW Iceland. Applied Geochemistry 21(9):1551–1569. https://doi.org/https://doi.org/10.1016/j.apgeochem.2006.04.006, URL https://www.sciencedirect.com/science/article/pii/S0883292706001235

Gaudin D, Finizola A, Delcher E, et al (2015) Influence of rainfalls on heat and steam fluxes of fumarolic zones: six months records along the Ty Fault (Soufrière of Guadeloupe, Lesser Antilles). J Volcanol Geoth Res 302:273–285. https://doi.org/10.1016/j.jvolgeores.2015.06.015, URL https://www.sciencedirect.com/science/article/pii/S0377027315001912

Gaudin D, Beauducel F, Coutant O, et al (2016) Mass and heat flux balance of La Soufrière volcano (Guadeloupe) from aerial infrared thermal imaging. Journal of Volcanology and Geothermal Research 320:107–116. https://doi.org/10.1016/j.jvolgeores.2016.04.007

Gaudin D, Ricci T, Finizola A, et al (2017) Heat flux-based strategies for the thermal monitoring of sub-fumarolic areas: Examples from Vulcano and La Soufrière de Guadeloupe. Journal of Volcanology and Geothermal Research 343:122–134. https://doi.org/10.1016/j.jvolgeores.2017.06.021

Grobbe N, Barde-Cabusson S (2019) Self-Potential Studies in Volcanic Environments: A Cheap and Efficient Method for Multiscale Fluid-Flow Investigations. International Journal of Geophysics 2019. https://doi.org/10.1155/2019/2985824

Harris A, Maciejewski A (2000) Thermal surveys of the vulcano fossa fumarole field 1994–1999: evidence for fumarole migration and sealing. Journal of Volcanology and Geothermal Research 102(1):119–147. https://doi.org/https://doi.org/10.1016/S0377-0273(00)00184-0, URL https://www.sciencedirect.com/science/article/pii/S0377027300001840

Harris AJL (2013) Thermal remote sensing of active volcanoes: a user's manual. Cambridge University Press

Harris AJL, Lodato L, Dehn J, et al (2009) Thermal characterization of the Vulcano fumarole field. Bull Volcanol 71(4):441–458. https://doi.org/10.1007/s00445-008-0236-8

Harvey MC, Rowland JV, Chiodini G, et al (2015) Heat flux from magmatic hydrothermal systems related to availability of fluid recharge. J Volcanol Geoth Res 302:225–236. https://doi.org/10.1016/j.jvolgeores.2015.07.003

Hase H, Ishido T, Takakura S, et al (2003) Zeta potential measurement of volcanic rocks from Aso caldera. Geophysical Research Letters 30(23). https://doi.org/https://doi.org/10.1029/2003GL018694, URL https://agupubs.onlinelibrary.wiley.com/doi/abs/10.1029/2003GL018694

Heap MJ, Troll VR, Kushnir AR, et al (2019) Hydrothermal alteration of andesitic lava domes can lead to explosive volcanic behaviour. Nature Communications 10. https://doi.org/10.1038/s41467-019-13102-8

Heap MJ, Kushnir AR, Vasseur J, et al (2020) The thermal properties of porous andesite. Journal of Volcanology and Geothermal Research 398:106901. https://doi.org/https://doi.org/10.1016/j.jvolgeores.2020.106901, URL https://www.sciencedirect.com/science/article/pii/S0377027320300925

Heap MJ, Baumann T, Gilg HA, et al (2021a) Hydrothermal alteration can result in pore pressurization and volcano instability. Geology 49:1348–1352. https://doi.org/10.1130/G49063.1

Heap MJ, Baumann TS, Rosas-Carbajal M, et al (2021b) Alteration-Induced Volcano Instability at La Soufrière de Guadeloupe (Eastern Caribbean). Journal of Geophysical Research: Solid Earth 126. https://doi.org/10.1029/2021JB022514

Heap MJ, Jessop DE, Wadsworth FB, et al (2022) The thermal properties of hydrothermally altered andesites from La Soufrière de Guadeloupe (Eastern Caribbean). J Volcanol Geoth Res 421:107444. https://doi.org/https://doi.org/10.1016/j.jvolgeores.2021.107444, URL https://www.sciencedirect.com/science/article/pii/S0377027321002730

Heap MJ, Wadsworth FB, Jessop DE (2023) The thermal conductivity of unlithified granular volcanic materials: The influence of hydrothermal alteration and degree of water saturation. J Volcanol Geoth Res 435:107775. https://doi.org/10.1016/j.jvolgeores.2023.107775, URL https://hal.uca.fr/hal-04005461v1

Hedenquist JW, Lowenstern JB (1994) The role of magmas in the formation of hydrothermal ore deposits. Nature 370(6490):519–527. https://doi.org/10.1038/370519a0

Hincks TK, Komorowski J, Sparks S, et al (2014) Retrospective analysis of uncertain eruption precursors at La Soufrière volcano, Guadeloupe, 1975–77: volcanic

hazard assessment using a Bayesian Belief Network approach. Journal of Applied Volcanology 3:1–26. https://doi.org/10.1186/2191-5040-3-3

Hirn A, Michel B (1979) Evidence of migration of main shocks during major seismo-volcanic crises of La Soufrière (Guadeloupe, Lesser Antilles) in 1976. Journal of Volcanology and Geothermal Research 6(3):295–304. https://doi.org/https://doi.org/10.1016/0377-0273(79)90007-6, URL https://www.sciencedirect.com/science/article/pii/0377027379900076

Hochstein MP, Bromley CJ (2005) Measurement of heat flux from steaming ground. Geothermics 34(2):131–158. https://doi.org/10.1016/j.geothermics.2004.04.002

Hochstein MP, Browne PRL (2000) Surface manifestations of geothermal systems with volcanic heat sources. In: Sigurdsson H, Houghton B, Rymer H, et al (eds) Encyclopedia of volcanoes, 1st edn. Academic Press, San Diego, p 835–855

Hutchison W, Mather TA, Pyle DM, et al (2015) Structural controls on fluid pathways in an active rift system: A case study of the Aluto volcanic complex. Geosphere 11(3):542–562. https://doi.org/https://doi.org/10.1130/GES01119.1, URL https://pubs.geoscienceworld.org/gsa/geosphere/article-pdf/11/3/542/3332882/542.pdf

Inostroza M, Moune S, Moretti R, et al (2022) Monitoring Hydrothermal Activity Using Major and Trace Elements in Low-Temperature Fumarolic Condensates: The Case of La Soufrière de Guadeloupe Volcano. Geosciences 12(7). https://doi.org/10.3390/geosciences12070267, URL https://www.mdpi.com/2076-3263/12/7/267

Jessop DE, Moune S, Moretti R, et al (2021) A multi-decadal view of the heat and mass budget of a volcano in unrest: La Soufrière de Guadeloupe (French West Indies). Bull Volcanol 83(3):16. https://doi.org/10.1007/s00445-021-01439-2, URL https://hal.uca.fr/hal-02974046v2

Jouniaux L, Ishido T (2012) Electrokinetics in earth sciences: A tutorial. International Journal of Geophysics 2012. https://doi.org/10.1155/2012/286107

Jouniaux L, Maineult A, Naudet V, et al (2009) Review of self-potential methods in hydrogeophysics. Comptes Rendus - Geoscience 341:928–936. https://doi.org/10.1016/j.crte.2009.08.008

Karstens J, Berndt C, Urlaub M, et al (2019) From gradual spreading to catastrophic collapse – Reconstruction of the 1888 Ritter Island volcanic sector collapse from high-resolution 3D seismic data. Earth and Planetary Science Letters 517:1–13. https://doi.org/10.1016/j.epsl.2019.04.009

Kilgour G, Manville V, Pasqua FD, et al (2010) The 25 September 2007 eruption of Mount Ruapehu, New Zealand: Directed ballistics, surtseyan jets, and ice-slurry lahars. J Volcanol Geoth Res 191:1–14. https://doi.org/10.1016/j.jvolgeores.2009.10.015

Komorowski JC, Boudon G, Semet M, et al (2005) Guadeloupe. In: Volcanic hazard atlas of the Lesser Antilles. Seismic Research Unit, the University of the West Indies, Trinidad and Tobago, W.I., p 65–102

Koretsky MD (2012) Engineering and Chemical Thermodynamics, 2nd edn., John Wiley & Sons, chap Appendix B: Steam Tables, pp 647–649

Lesparre N, Gibert D, Marteau J, et al (2012) Density muon radiography of La Soufrière of Guadeloupe volcano: comparison with geological, electrical resistivity and gravity data. Geophysical Journal International 190(2):1008–1019. https://doi.org/https://doi.org/10.1111/j.1365-246X.2012.05546.x, URL https://onlinelibrary.wiley.com/doi/abs/10.1111/j.1365-246X.2012.05546.x

Lewicki JL, Connor C, St-Amand K, et al (2003) Self-potential, soil CO2 flux, and temperature on Masaya volcano, Nicaragua. Geophysical Research Letters 30. https://doi.org/10.1029/2003GL017731

Lewis A, Hilley GE, Lewicki JL (2015) Integrated thermal infrared imaging and structure-from-motion photogrammetry to map apparent temperature and radiant hydrothermal heat flux at Mammoth Mountain, CA, USA. J Volcanol Geoth Res 303:16–24. https://doi.org/10.1016/j.jvolgeores.2015.07.025

Lénat JF (2007) Retrieving Self Potential anomalies in a complex volcanic environment : a SP/elevation gradient approach. Near Surface Geophysics 5:161–170. https://doi.org/10.3997/1873-0604.2006028

López DL, Williams SN (1993) Catastrophic volcanic collapse: Relation to hydrothermal processes. Science 260:1794–1796. https://doi.org/10.1126/science.260.5115.1794

Maeno F, Nakada S, Oikawa T, et al (2016) Reconstruction of a phreatic eruption on 27 September 2014 at Ontake volcano, central Japan, based on proximal pyroclastic density current and fallout deposits the Phreatic Eruption of Mt. Ontake Volcano in 2014 5. Volcanology. Earth, Planets and Space 68. https://doi.org/10.1186/s40623-016-0449-6

Massenet F, Pham VN (1985) Mapping and surveillance of active fissure zones on a volcano by the self-potential method, Etna, Sicily. Journal of Volcanology and Geothermal Research 24(3):315–338. https://doi.org/https://doi.org/10.1016/0377-0273(85)90075-7, URL https://www.sciencedirect.com/science/article/pii/0377027385900757

Matsushima N, Michiwaki M, Okazaki N, et al (1990) Self-Potential Studies in Volcanic Areas(2) : Usu, Hokkaido Komaga-take and Me-akan. Journal of the Faculty of Science, Hokkaido University Series 7, Geophysics 8:465–477. URL https://www.researchgate.net/publication/37548954

Metcalfe A, Moune S, Komorowski JC, et al (2022) Bottom-up vs top-down drivers of eruption style: Petro-geochemical constraints from the holocene explosive activity at La Soufrière de Guadeloupe. Journal of Volcanology and Geothermal Research 424:107488. https://doi.org/https://doi.org/10.1016/j.jvolgeores.2022.107488, URL https://www.sciencedirect.com/science/article/pii/S0377027322000191

Metcalfe A, Moune S, Moretti R, et al (2023) Volatile emissions from past eruptions at La Soufrière de Guadeloupe (Lesser Antilles): insights into degassing processes and atmospheric impacts. Frontiers in Earth Science 11. https://doi.org/10.3389/feart.2023.1143325, URL https://www.frontiersin.org/articles/10.3389/feart.2023.1143325

Moretti R, Komorowski JC, Ucciani G, et al (2020a) The 2018 unrest phase at La Soufrière of Guadeloupe (French West Indies) andesitic volcano: Scrutiny of a failed but prodromal phreatic eruption. J Volcanol Geoth Res 393. https://doi.org/10.1016/j.jvolgeores.2020.106769

Moretti R, Moune S, Robert V, et al (2020b) Intercomparison of geochemical techniques at La Soufrière de Guadeloupe (FWI) volcano: their advantages and their limits over a long-standing unrest. Ital J Geosci https://doi.org/10.3301/IJG.2020.13, URL https://hal.archives-ouvertes.fr/hal-03092221v1

Moune S, Moretti R, Burtin A, et al (2022) Gas monitoring of volcanic-hydrothermal plumes in a tropical environment: the example of La Soufrière de Guadeloupe unrest volcano (Lesser Antilles). Frontiers in Earth Science 10. https://doi.org/10.3389/feart.2022.795760, URL https://hal.uca.fr/hal-03609801v1

Nourbehecht B (1963) Irreversible Thermodynamic Effects in Inhomogeneous Media and Their Application in Certain Geoelectric Problems. PhD thesis, Massachusetts Institute of Technology

OVSG-IPGP (1992–2023) Bilans mensuels et annuels de l'activité volcanique de la Soufrière de Guadeloupe et de la sismicité régionale. In: Annual and monthly activity reports. Observatoire Volcanologique et Sismologique de la Guadeloupe

Pham V, Boyer D, Boudon G, et al (1990) Anomalies de polarisation spontanée sur La Soufrière de Guadeloupe. Relation avec la structure interne du volcan. C R Acad Sci 2:815–821

Pichavant M, Poussineau S, Lesne P, et al (2018) Experimental Parametrization of Magma Mixing: Application to the AD 1530 Eruption of La Soufrière, Guadeloupe (Lesser Antilles). Journal of Petrology 59:257–282. https://doi.org/10.1093/petrology/egy030

Pritchard ME, Mather TA, McNutt SR, et al (2019) Thoughts on the criteria to determine the origin of volcanic unrest as magmatic or non-magmatic. Philosophical Transactions of the Royal Society A: Mathematical, Physical and Engineering

Sciences 377. https://doi.org/10.1098/rsta.2018.0008

Reid M, Sisson T, Brien D (2001) Volcano collapse promoted by hydrothermal alteration and edifice shape, Mount Rainier, Washington. Geology 29. https://doi.org/10.1130/0091-7613(2001)029⟨0779:VCPBHA⟩2.0.CO;2

Reid ME (2004) Massive collapse of volcano edifices triggered by hydrothermal pressurization. Geology 32:373–376. https://doi.org/10.1130/G20300.1

Remy N, Boucher A, Wu J (2009) Applied Geostatistics with SGeMS: A User's Guide. Cambridge University Press, https://doi.org/https://doi.org/10.1017/CBO9781139150019

Revil A (2002) Comment on "Rapid fluid disruption: A source for self-potential anomalies on volcanoes" by M. J. S. Johnston, J. D. Byerlee, and D. Lockner. Journal of Geophysical Research 107. https://doi.org/10.1029/2001jb000788

Revil A, Gresse M (2021) Induced polarization as a tool to assess alteration in geothermal systems: A review. Minerals 11(9). https://doi.org/10.3390/min11090962, URL https://www.mdpi.com/2075-163X/11/9/962

Revil A, Schwaeger H, Cathles LM, et al (1999) Streaming potential in porous media 2. Theory and application to geothermal systems. Journal of Geophysical Research: Solid Earth 104:20033–20048. https://doi.org/10.1029/1999jb900090

Revil A, Finizola A, Gresse M (2023) Self-potential as a tool to assess groundwater flow in hydrothermal systems: A review. Journal of Volcanology and Geothermal Research 437:107788. https://doi.org/https://doi.org/10.1016/j.jvolgeores.2023.107788, URL https://www.sciencedirect.com/science/article/pii/S0377027323000458

Ricci T, Finizola A, Barde-Cabusson S, et al (2015) Hydrothermal fluid flow disruptions evidenced by subsurface changes in heat transfer modality: The La Fossa cone of Vulcano (Italy) case study. Geology 43:959–962. https://doi.org/10.1130/G37015.1

Rosas-Carbajal M, Komorowski JC, Nicollin F, et al (2016) Volcano electrical tomography unveils edifice collapse hazard linked to hydrothermal system structure and dynamics. Scientific Reports 6. https://doi.org/10.1038/srep29899

Rouwet D, Sandri L, Marzocchi W, et al (2014) Recognizing and tracking volcanic hazards related to non-magmatic unrest: A review. Journal of Applied Volcanology 3. https://doi.org/10.1186/s13617-014-0017-3

Salaün A, Villemant B, Gérard M, et al (2011) Hydrothermal alteration in andesitic volcanoes: Trace element redistribution in active and ancient hydrothermal systems of Guadeloupe (Lesser Antilles). Journal of Geochemical Exploration 111:59–83.

https://doi.org/10.1016/j.gexplo.2011.06.004

Schöpa A, Pantaleo M, Walter T (2011) Scale-dependent location of hydrothermal vents: Stress field models and infrared field observations on the Fossa Cone, Vulcano Island, Italy. Journal of Volcanology and Geothermal Research 203(3):133–145. https://doi.org/https://doi.org/10.1016/j.jvolgeores.2011.03.008, URL https://www.sciencedirect.com/science/article/pii/S0377027311000813

Sinclair AJ (1974) Selection of threshold values in geochemical data using probability graphs. Journal of Geochemical Exploration 3:129–149. https://doi.org/10.1016/0375-6742(74)90030-2, URL https://www.sciencedirect.com/science/article/pii/0375674274900302

Sparks RS, Barclay J, Calder ES, et al (2002) Generation of a debris avalanche and violent pyroclastic density current on 26 December (Boxing Day) 1997 at Soufrière Hills Volcano, Montserrat. Geological Society Memoir 21:409–434. https://doi.org/10.1144/GSL.MEM.2002.021.01.18

Stevenson DS (1993) Physical models of fumarolic flow. J Volcanol Geoth Res 57(3–4):139–156. https://doi.org/10.1016/0377-0273(93)90009-G

Tamburello G, Moune S, Allard P, et al (2019) Spatio-temporal relationships between fumarolic activity, hydrothermal fluid circulation and geophysical signals at an arc volcano in degassing unrest: La Soufrière of Guadeloupe (French West Indies). Geosci 9(11). https://doi.org/10.3390/geosciences9110480

Vaerewyck C (2022) Évolution géochimique du lac acide Tarissan, Soufrière de Guadeloupe: couplage à la modélisation hydrogéologique pour l'interprétation des variations temporelles des concentrations en éléments halogènes. Master's thesis, Institut de Physique du Globe de Paris (IPGP), Université Paris Cité

Villemant B, Komorowski JC, Dessert C, et al (2014) Evidence for a new shallow magma intrusion at La Soufrière of Guadeloupe (Lesser Antilles). Insights from long-term geochemical monitoring of halogen-rich hydrothermal fluids. J Volcanol Geoth Res 285:247–277. https://doi.org/10.1016/j.jvolgeores.2014.08.002

van Wyk de Vries B, Francis P (1997) Catastrophic collapse at stratovolcanoes induced by gradual volcano spreading. Nature 387:387–390. https://doi.org/10.1038/387387a0

Watters R, Zimbelman D, Bowman S, et al (2000) Rock Mass Strength Assessment and Significance to Edifice Stability, Mount Rainier and Mount Hood, Cascade Range Volcanoes. Pure and applied geophysics 157:957–976. https://doi.org/10.1007/s000240050012

Zlotnicki J, Boudon G, Le Mouël JL (1992) The volcanic activity of La Soufrière of Guadeloupe (Lesser Antilles): structural and tectonic implications. J Volcanol Geoth

Res 49(1):91–104. https://doi.org/10.1016/0377-0273(92)90006-Y

Zlotnicki J, Feuillard M, Hammouya G (1994) Water Circulations on La Soufrière Volcano Inferred by Self-Potential Surveys (Guadeloupe, Lesser Antilles). Renew of Volcanic Activity ? J Geomag Geoelectr 46:797–813